MECHANISM AND EXPERIMENTAL VALIDATION OF SELF-CENTERING NONLINEAR FRICTION DAMPER

by

Xi Zuo

B.Eng., Jiangnan University, 2017

A THESIS SUBMITTED IN PARTIAL FULFILLMENT OF

THE REQUIREMENTS FOR THE DEGREE OF

MASTER OF APPLIED SCIENCE

in

THE FACULTY OF GRADUATE AND POSTDOCTORAL STUDIES

(Civil Engineering)

THE UNIVERSITY OF BRITISH COLUMBIA

(Vancouver)

September 2020

The following individuals certify that they have read, and recommend to the Faculty of Graduate and Postdoctoral Studies for acceptance, a thesis entitled:

Mechanism and Experimental Validation of Self-Centering Nonlinear Friction Damper

submitted by	Xi Zuo	in partial fulfillment of the requirements for
the degree of	Master of Applied Science	
in	Civil Engineering	

Examining Committee:

Tony T.Y. Yang, Department of Civil Engineering, University of British Columbia
Supervisor

Yao Cui, Department of Civil Engineering, Dalian University of Technology
Additional Examiner

Abstract

Current earthquake design philosophy in North America focuses on providing minimum "life safety" requirement, where main structural components are designed to dissipate the earthquake energy through inelastic yielding during strong earthquake shaking. This could result in significant financial losses and downtime. The next-generation seismic design focuses on the use of energy dissipation devices which forces the earthquake energy dissipation in specially designed devices, while majority of the structures are capacity protected to be damage free. Hence, structure can be inspected or repaired efficiently after earthquake. To make the structure even more resilient, newer high-performance structures are designed to have low residual drift after the earthquake, hence the structures can be used shortly or immediately after strong earthquake. In this thesis, a novel self-centering energy dissipation device, named self-centering nonlinear friction damper (SCNFD), is proposed. SCNFD utilizes pivot hinge, specially designed grove plates and pre-compressed springs to create self-centering nonlinear elastic force-deformation response. In addition, friction pads are added to create the energy dissipation needed. Detailed theoretical equations were derived to describe the mechanical behavior of the SCNFD. The behavior of the SCNFD was validated using nine experimental tests. The results show the behavior of SCNFD can be well modeled using the theoretical equations presented in this thesis. Finally, a detailed parameter study on the stiffness of springs, pre-compressed force, friction and pivot plate ratio have been calculated to evaluate their effects on the hysteretic response of the SCNFD. Results demonstrate different flag-shaped hysteresis responses can be achieved using different SCNFD configurations, which make SCNFD a versatile, reliable and efficient damper for seismic applications.

Lay Summary

In this thesis, a novel self-centering friction damper named self-centering nonlinear friction damper (SCNFD) has been introduced. Detailed theoretical equation of the SCNFD has been derived. The behavior of the SCNFD has been verified using experimental tests. The result shows SCNFD has stable force-deformation response and it can be reliably estimated using the theoretical equations presented. Finally, a detailed parameter study was conducted to examine the influence of SCNFD geometry and mechanical property on the force-deformation response of SCNFD. The result shows SCNFD can be designed to fit various seismic demands. Hence, SCNFD can be used as a versatile and reliable energy dissipation device for seismic engineering application.

Preface

The initial idea for this research was proposed by Professor T.Y. Yang, Professor Geoffrey Rodgers, the author and Fabrício Bagatini Cachuço. The author of this research was responsible of the literature review, mathematical and finite element modeling, experimental test, data processing, results and conclusion. The experimental part was conducted by using test set up at the University of British Columbia and the ACTS control system. This thesis has been written by the author and revised by Professor T.Y. Yang at the Department of Civil Engineering at the University of British Columbia, Vancouver. Part of this thesis has been summarized into a journal paper which is currently under review.

Table of Contents

List of Tables

List of Figures

List of Symbols

α = Rotation angle of pivot plate

β_1 = Rotation angle of spring case 1

β_2 = Rotation angle of spring case 2

a = Geometric parameter of pivot plate (Horizontal direction)

b = Geometric parameter of pivot plate (Vertical direction)

D_x = Horizontal displacement

D_y = Vertical displacement

F_f = Friction force

F_1= Force in Spring Case 1

F_2= Force in Spring Case 2

k = Spring stiffness

kp = Post yield stiffness of SCNFD

L = Initial length of Spring Case 1 and 2

N = Clamping force on bolt.

P = Shear force of SCNFD

P_c = Pre-compress load on the springs inside the Spring Cases

P_0 = Initial sliding force of SCNFD

P_m = Maximum sliding force of SCNFD

P_u = Unloading sliding force of SCNFD

P_r = Residue force of SCNFD

$\triangle$ = Vertical displacement of SCNFD

δ = Drift ratio of SCNFD

γ = b/a = Geometric ratio of the pivot plate

μ = Friction coefficient

List of Abbreviations

ADAS: Added damping and stiffness

AFC: Asymmetrical Friction Connections

Al-STD: Aluminum shear-yielding damper

ESFP: Equivalent Static Force Procedure

FBD: Free body diagram

HSF: Honeycomb structural fuse

LP: Linear pot

MYD: Metallic yielding damper

PS-SCED: Pre-pressed spring self-centering energy dissipation

RC: Reinforced concrete

SCNFD: Self-centering nonlinear friction damper

SFC: Symmetrical Friction Connections

SFR: Sliding friction rubber

SMA: Shape-memory alloy

SSD: Steel slit damper

Acknowledgements

First, I would like to gratefully acknowledge my supervisor, Prof. T.Y. Yang at the Department of Civil Engineering at the University of British Columbia, Vancouver. His patience and valuable suggestions have contributed greatly to the research. Without his painstaking efforts in revising and polishing my drafts, the completion of the present thesis would not have been possible. He gave me the opportunity to conduct this great research and understand the meaning of seismic engineering.

Meanwhile, I would like to thank Prof. Rodgers for his idea on optimizing the SCNFD design. He helped us to optimize the SCNFD from a complicated damper to a concise one. Besides, He did a lot of detailed work to manufacture the device. I really appreciate for his patience and carefully checking.

I also want to express my gratitude to my research colleague Fabrício Bagatini Cachuço, who has given me tremendous assistance in developing the mechanism of SCNFD. His organized research method and passion on investing the seismic protection device impressed me a lot.

Furthermore, I would like to thank my other research colleagues, Tiangyang Qiao, Tianyi Li, Henry Xu, Xiao Pan, Lisa Tobber, Soham Vaze, Lan Yang and Hollis Yao for their help. Also, my friends, Ziyu Song, Yimeng Liu, Andy Wu, Slow Zhuo, Tianyi Liu, Weijun Zeng, thank you for bringing the happiness and encouragement to me, that would be the precious memory for me.

Most of all, special thanks go to my parents. They are the model for me in persistence and conscientious. Their unconditional love and support make me confident and optimistic.

Dedication

This thesis is dedicated with love, gratitude and deep appreciation to my mother and father.

Chapter 1: Introduction

1.1 Background

Earthquake has been a major reason to structure damage, which has resulted to both economy and human life losses. Engineers have proposed several methods to avoid severe damage to structures during earthquakes. The current design philosophy has been identified on the adequacy for determining the earthquake load (Tremblay et al., 2005) to avoid the collapse in structures. However, the philosophy allows elements yielding which leads to permanent plastic deformations and out-of-plumb drifts. Thus, even the philosophy is followed strictly, the structure damage and economic losses still cannot be avoided. Concerning the earthquake happened in recent years, for example, in Chiapas Mexico (2017), a 8.2 magnitude earthquake caused 41,000 homes damaged, buildings close to the epicenter were “reduce to rubble” and the economic losses was 440 billion USD; A magnitude 7.8 earthquake rocked Ecuador (2016), more than 35,000 houses were destroyed; Another major magnitude 8.3 earthquake struck Chile (2015), caused 40 billion USD losses in economic and insured. It seems following the conventional design will lead to costly repair. With the objective to minimize down time and repair cost, a new generation of passive energy dissipation (PED) system have been explored (Soong, 1997, Tehranizadeh, 2001, Lin et al., 2003, Xu et al., 2007). PED has become one of the most effective methods to eliminates tructure damage and limits the financial losses. Widely used PEDs are yielding damper, viscous damper and friction damper. Sahoo (2009) carried out experimental tests on a reduced scale reinforced concrete (RC) frame with the aluminum shear-yielding damper (Al-SYD). The Al-SYD was made of alloy-1100 and formed by welding aluminum plates for flanged, web and transverse stiffeners. During tests, the web plate of the Al-SYD underwent shear deformation. A large amount of energy was dissipated because of low-yield strength and post-yield hardening behavior of aluminum plates. However, the yielding leads to residual deformation which may result in loss of operation efficiency of structures. Other studies on yielding dampers also indicated the stable energy dissipation behavior but without self-centering property (Mahyari et al., 2019, Garivani et al., 2018). Viscous dampers have been subjected to many experimental and numerical investigations (Symans et al., 1995, Hazaveh et al., 2017). Naeem (2018) tried to improve the behavior of the viscous damper by using an external spring. Thus, the viscous damping system is self-centering and has good energy dissipation capacity. However, the leakage remains in viscous dampers. Friction damper is one of the most economical dampers with stable energy dissipation character. Ibrahim (1994) studied the comparison of energy dissipated capacity of friction damper and viscous damper, results showed the former is larger that the latter. Other studies upgraded the simple energy dissipated behavior to a self-center and energy dissipated behavior by using springs, rubbers and post-tension bars (Ricles et al., 2001, Garlock et al., 2005, Chi et al., 2012, Khoo et al., 2012). However, the friction damper with springs has a constant post stiffness due to the stiffness of mechanical springs. In other words, the force keeps increase with increasing deformation. This behavior may cause damage to structure and make it difficult for the connection to be capacity designed. The friction damper with rubbers can not self center immediately due to the viscoelastic property of rubbers. What's more, the friction damper with post-tension bars has undesirable interaction during earthquake. To improve the behavior of friction dampers, a novel damper named self-centering nonlinear friction damper (SCNFD) is proposed in this thesis. The hysteresis curve is nonlinear due to nonlinear geometric transformation. In this way, the damper is protected with limited force. During the earthquake, the SCNFD is damage free and can go back to initial state immediately. Concept, theoretical equations and are presented to describe the nonlinear behavior of the SCNFD. Experimental tests were conducted to exam the force-deformation response of the SCNFD. The experimental results were used to verify the theoretical equation presented. The result shows the behavior of SCNFD can match the experimental observation very well. Detailed parameter study was conducted using theoretical equations. The result shows that SCNFD can achieve different behaviors using different configurations. Hence, it can be used as a versatile PED for seismic application.

1.2 Review of conventional control devices

1.2.1 Metallic damper

Metallic damper dissipate energy when undergoing inelastic deformation. It has the advantage of low fabrication cost and stable energy dissipated behavior. Kelly (1972) first introduced the idea of MYD into a building structure to consume input seismic energy. Over the past four decades, X-shaped plate damper and ADAS (added damping and stiffness) have received considerable attention. They are made with X-shaped or triangular plates, spaced by rectangular steel plates and assembled to end blocks by bolts or wielding. Figure 1.1 shows the device. By the application of ADAS, more input seismic energy is absorbed because of the increased damping.

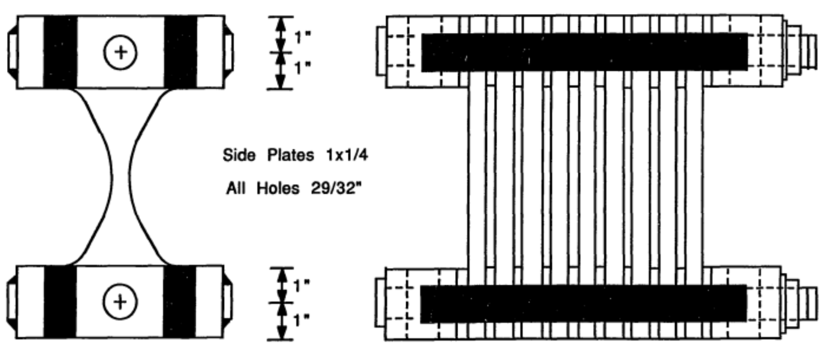

Figure 1.1 ADAS device (Su 1990)

In recent research, experimental and numerical evaluations of the retrofitted of concrete moment resisting frames with ADAS yielding dampers were carried out by TahamouliRoudsari (2019). As shown in Figure 1.2, the frame was tested with 4 ADAS plates by applying the load in weak axis. And the hysteretic energy was achieved through the flexural yielding of steel plates. The hysteresis diagram indicated the stable energy dissipation capacity of ADAS. An important parameter, the number of ADAS plates was mentioned in the numerical study. The low number of ADAS plates leads to minimal increasement of stiffness and strength, which causes not suitable performance. The high number of ADAS plates leads to higher stiffness and force capacity. However, if the number is too high, it may not yield and cause damage to structure.

Figure 1.2 Reinforced concrete frame experimental modal with 4 ADAS plates (TahamouliRoudsari, 2019)

Steel slit damper (SSD) has been investigated in recent years, which relies on the inelastic shear deformation of metallic plate under the load in strong axis. Chan (2008) carried out the study on the energy dissipative capacity of SSD. Shown in Figure 1.3. The results showed the SSD is capable of dissipating significant amounts of energy. And parameter study mentioned that, longer and wider slits cause the device more flexible, and short or narrow slits lead to higher stiffness but make the device suffer from earlier failure.

Figure 1.3 Steel slit damper (Chan and Albermani 2008)

Bing (2019) conducted experimental tests on the damper consisting of the replaceable U-shaped plates as the energy dissipating elements. In Figure 1.4, one side of each U-shaped steel plate is bolted to the piston element; the other side is bolted to the casing element. During the test, the longitudinal cyclic displacement was applied to the piston element, keeping the casing elements stationary. The damper dissipated energy through flexural yielding of the U-shaped steel plates. The experimental results showed the U-shaped plate exhibit a stable hysteretic behavior. On the other hand, the strength of the damper increases with the increasing of the thickness of the U-shaped steel plates.

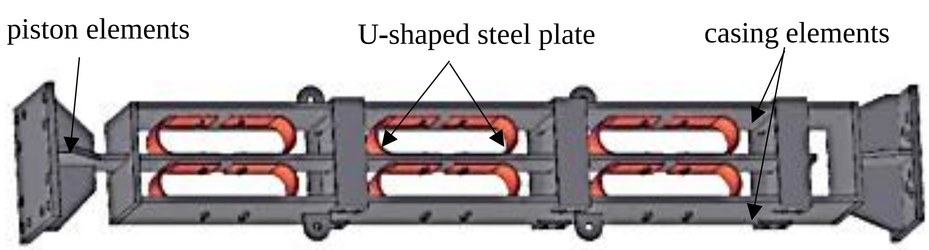

Figure 1.4 Detailed information of the damper (Bing 2019)

Another worth mentioned shear damper study was conducted (Yang et al., 2018), shown in Figure 1.5. An innovate honeycomb fuse (HSF) was designed with different pattern of honeycomb shaped holes. Nine specimens with different hole pattern were tested. The experimental results showed that, the HSF with low cell wall aspect ratio has more stable hysteresis curve, while HSF with higher cell wall aspect ratio has more pinched behavior. And with the increases of cell wall aspect ratio, the failure mode of HSF transfers from local cell bending to the global plate buckling.

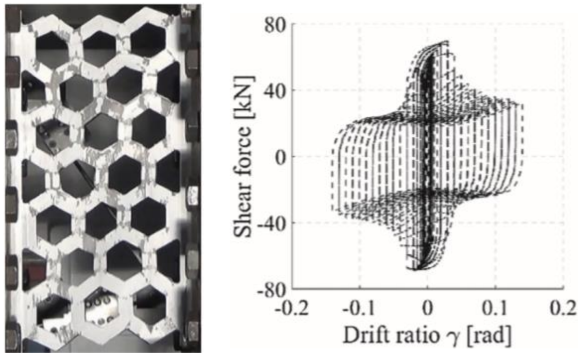

Figure 1.5 Honeycomb fuse (Yang, et al 2018)

One other kind of the metallic damper is the shape-memory alloy (SMA). Due to its micromechanical phase transition, SMA has the capacity to go through big strains and recover to its initial status by inelastic deformation. This large energy-absorbing property makes SMA an ideal material for seismic protection. Graesser (1991) introduced SMA into civil engineering field. However, the favorable self-centering and energy dissipated features depend on temperature. Figure 1.6 shows the behavior of SMA under different temperatures, where M_f is the temperature at which the microstructure is fully martensitic. The temperature in structure is hard to be controlled. On the other hand, SMA is expensive and difficult to machine.

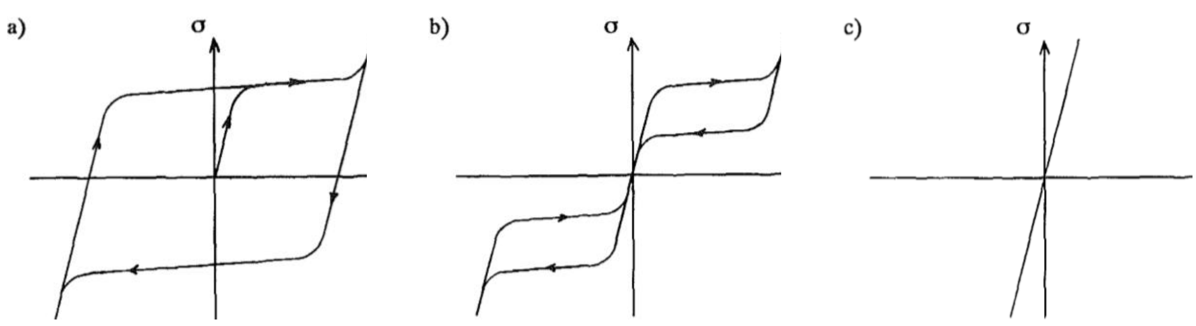

T < M_f T > M_f T » M_f

Figure 1.6 Stress-strain curve for SMA under different temperature (Graesser et al.,1991)

1.2.2 Viscous damper

Viscous dampers dissipate energy through the displacement and velocity of fluid (Hazaveh et al., 2017; Naeem et al., 2018), and it was initially applied in the military and aerospace industry. It has been introduced into structural engineering in 1990s. Usually, viscous damper consists of a piston with orifices contained in a cylinder filled with highly viscous fluid. As shown in Figure 1.7. When the relative motion happens in the damper, the fluid is pushed or pulled by piston. By this way, a large force generated to resist the relative motion. Even though the experimental results showed the viscous damper is capable of absorbing significant amounts of seismic energy (Symans et al., 1998), the fluid leakage remains an ongoing challenge.

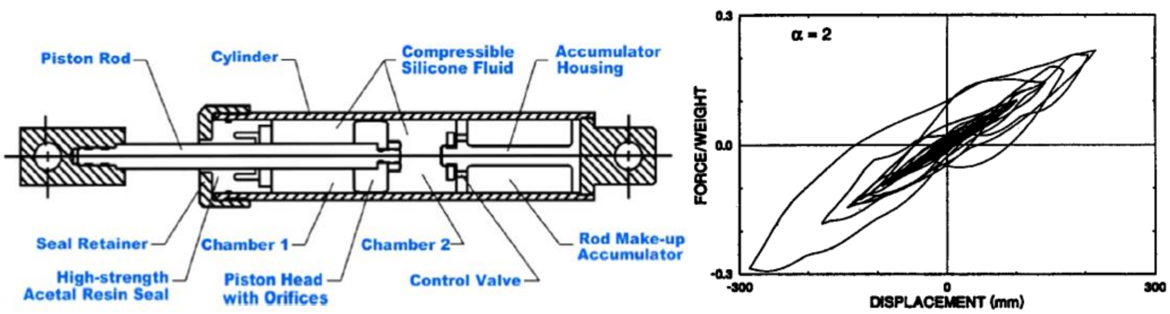

Figure 1.7 Viscous damper and its behavior (Symans et al., 1998)

1.2.3 Friction damper

As one of the most popular dampers, friction damper has advantages such as simple mechanism, low cost, and adequate energy dissipation capacity. It has been widely implemented not only for the seismic design but also for the rehabilitation and seismic upgrade of existing structures. Pall (1982) proposed the Symmetrical Friction Connections (SFC) to dissipate energy in moment resisting frame buildings. SFC comprises of two steel outside plates and one steel inner plate. The plates are connected using structural bolts. To allow the inner plate to move in and out of the device, slotted holes have been made on the inner plate. Engineers can then tighten the bolts to modify the normal force applied on the inner plate. Hence, adjust the friction force in the SFC. The analytical and experimental results show that the SFC has stable Coulomb friction hysteresis. (Den Hartog et al., 1931; Levitan et al., 1960; Hundal, 1979). Clifton (2005) introduced the Asymmetrical Friction Connections (AFC) in moment resisting frames by combining a steel slotted plate with a set of friction shims that are attached by high strength bolts. As shown in Figure 1.8. The mechanism dissipates energy through friction at the shims by overcoming the shear force caused by the clamping force of bolts. As a result, the hysteresis loops are stable and rectangular.

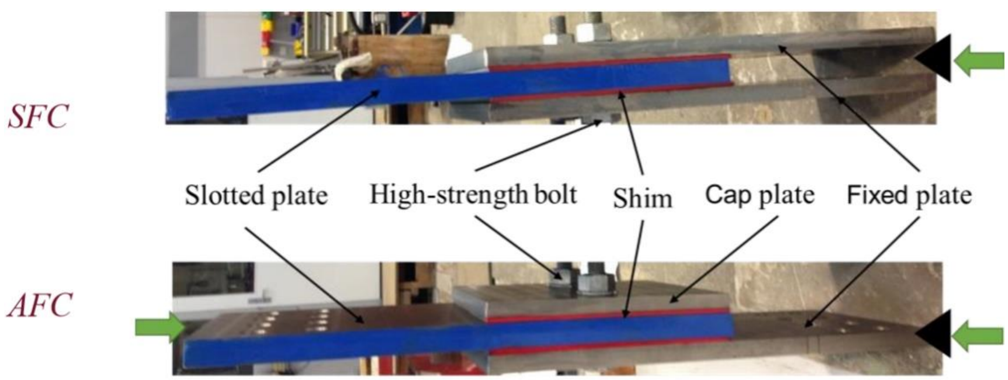

Figure 1.8 SFC and AFC components (Hatami et al., 2019)

Mualla (2002) identified that the choice of proper friction pad materials is crucial to obtain a stable hysteric behavior and recommended usage of materials with high hardness feature, such as Bisalloy 500 shims (Golondrino et al., 2012). However, the disadvantage of those friction damper is the offset between sliding components, which may lead to residual deformations in the structural system after the earthquake shaking. To tackle this undesirable feature, rubbers, PT tendons and springs have been used together with friction pads. Jeong (2016) developed sliding friction rubber (SFR) damper by combining the slip friction of aramid brake lining and the self-centering property of pre-compressed rubber springs. As shown in Figure 1.9, No.1 and No.2 mean rubber spring with restoring capacity, while No.3 and No.4 represent the aramid brake lining. The rubber spring deforms in axial compressive direction and brake lining resists the sliding in both directions. The damper can behave as self-centering as long as the pre-compressed force of rubber spring is larger than the friction force. Dynamic tests were conducted with different loading frequencies and friction forces. The results showed a flag-shaped hysteretic curve. However, because of the viscoelastic property, the rubber spring did not recover to their initial state immediately. More recently, Xu (2018) improved the behavior of the SFR by replacing the rubber springs with mechanical springs. He named the new device proposed pre-pressed spring self-centering energy dissipation (PS-SCED) bracing system, shown in Figure 1.10. No matter the outer tube is moving to the left or to the right, the inside spring always make the outer tube move back to the initial state. Numerical and experimental studies show that the PS-SCED can provided self-centering capability. At the same time, the force-deformation response of PS-SCED is rate independent. One of the major deficiencies of PS-SCED lies in the mechanical property of the mechanical spring. As the mechanical springs inside the PS-SCED are designed to remain linear, the force-deformation response of the PS-SCED is expected to increase as the deformation increase. Such elastic "post yield" stiffness could cause high forces in the device. Hence, it may be difficult to capacity design the connection.

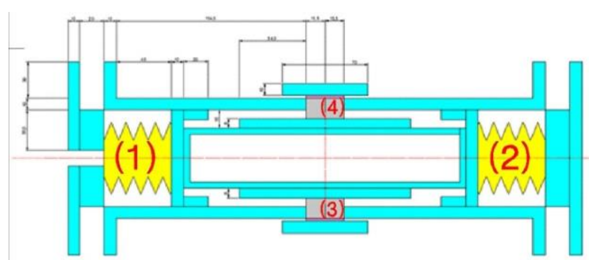

Figure 1.9 Concept of the SFR damper (Jeong et al., 2016)

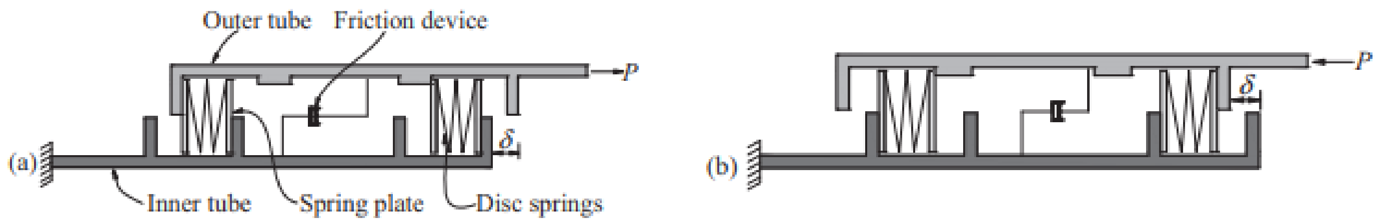

Figure 1.10 Working principle of the PS-SCED brace (Xu et al., 2018)

Kim (2008) proposed a friction posttensioned self-centering connection (Figure 1.11), which is usually used at the column base or between beam and column. This connection incorporates friction pads, posttensioned bars and the backbone frame. The energy dissipation capability is obtained by friction pads while the posttensioned bars provides the self-centering capacity. Experimental and numerical studies were carried out showing agreement on results, where device is capable of providing a flag-shaped response. Similarly, Zhang (2016) carried out an experimental study on prefabricated post-tension self-centering beam-column connections. The result showed the self-centering behavior with high energy dissipation capacity. Researchers also found that the maximum gap opening rotation and energy-dissipation decrease with the increase of initial post-tension force. However, authors mentioned that the "gap-opening" leads to undesirable interaction between gravity and lateral system that cause damage on the slabs.

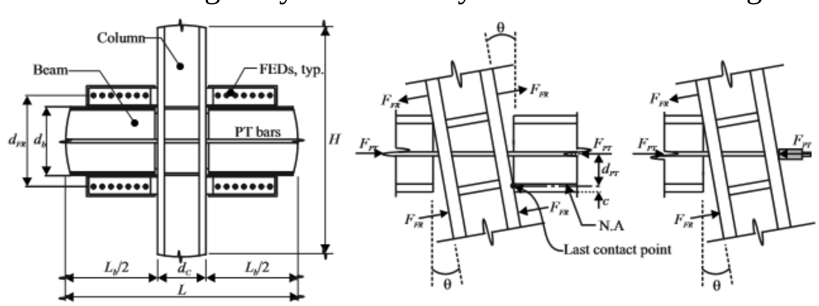

Figure 1.11 Self-centering friction connection (Kim et al., 2008)

1.3 Limitation of previous studies

Self-centering and energy dissipation damper using pre-load springs or post-tensioned bars as the self-centering device had been studied as some of these researches were presented in the above sections. The results showed this kind of mechanism can provide a stable self-centering mechanism. However, these studies showed some limitations in applications.

In general, the spring in self-centering damper deforms in their elastic range, thus the post stiffness is a constant value. In other words, the forces increase linearly with the increase of deformation. Hence, it is difficult to capacity design the connections. On the other hand, the self-centering connections using post-tensioned bars usually have interaction between columns and beams. Thus, the damage on the connection cannot be avoided.

1.4 Scope of work

The research in this thesis has four main objects:

- The first objective is to propose a new self-centering and energy dissipation damper. Deriving the theoretical equations and conducting finite element model for the self-centering mechanism.
- The second objective is to conduct individual component and overall damper experimental tests to validate the behavior and theoretical equations of SCNFD.
- The third objective is to carry out detailed parameter study by using the verified theoretical equations, to study the influence on the SCNFD parameters on the nonlinear hysteresis behavior.
- The fourth objective is to present a design procedure for SCNFD.

1.5 Organization of thesis

Chapter 1 presents the introduction and literature review of SCNFD.

Chapter 2 explains the detailed mechanism of SCNFD. Detailed theoretical equations of nonlinear flag-shaped hysteretic behavior of the SCNFD are presented. In addition, numerical model in Abaqus is presented. Comparison of the theoretical equation and Abaqus result is presented.

Chapter 3 focuses on the overall damper experiment test. Test setup, instrumentation details, loading protocol and controller are summarized. Test results are compared with theoretical equations.

Chapter 4 presents the parameter study by investigating the nonlinear behavior with changes of the pre-compressed load on spring, the initial length of spring case, the spring stiffness and pivot plate dimensions

Chapter 5 summaries conclusions of the study and future research recommendation.

Chapter 2: Mechanism of SCNFD

Self-centering damper has attracted lots of attentions in seismic engineering in recent years. This chapter introduces a new self-centering damper, named self-centering nonlinear friction damper (SCNFD). Theoretical equations for the mechanism of the SCNFD are derived. The mechanism is verified using finite element model in Abaqus. The result shows SCNFD has self-center mechanism with stable energy dissipation mechanism.

2.1 Self-centering nonlinear friction damper (SCNFD)

In this thesis, a novel self-centering nonlinear friction damper (SCNFD) is proposed. An exemplary embodiment of SCNFD is illustrated in Figure 2.1. There are four important characteristics attributed to the SCNFD: self-centering; adequate energy dissipation capacity; damage free and limited post-yield force due to the non-linear geometry transformation of the mechanism. The SCNFD does not require replacement after strong shaking events and it also can be easily calibrated to attend different seismic performances. The SCNFD represents a significant advance on structural and earthquake engineering, as it attends the current demands for efficient resilient structural systems. Figure 2.2 shows a potential application of SCNFD. In this example, the friction damper is used as coupling beam in coupled shear wall.

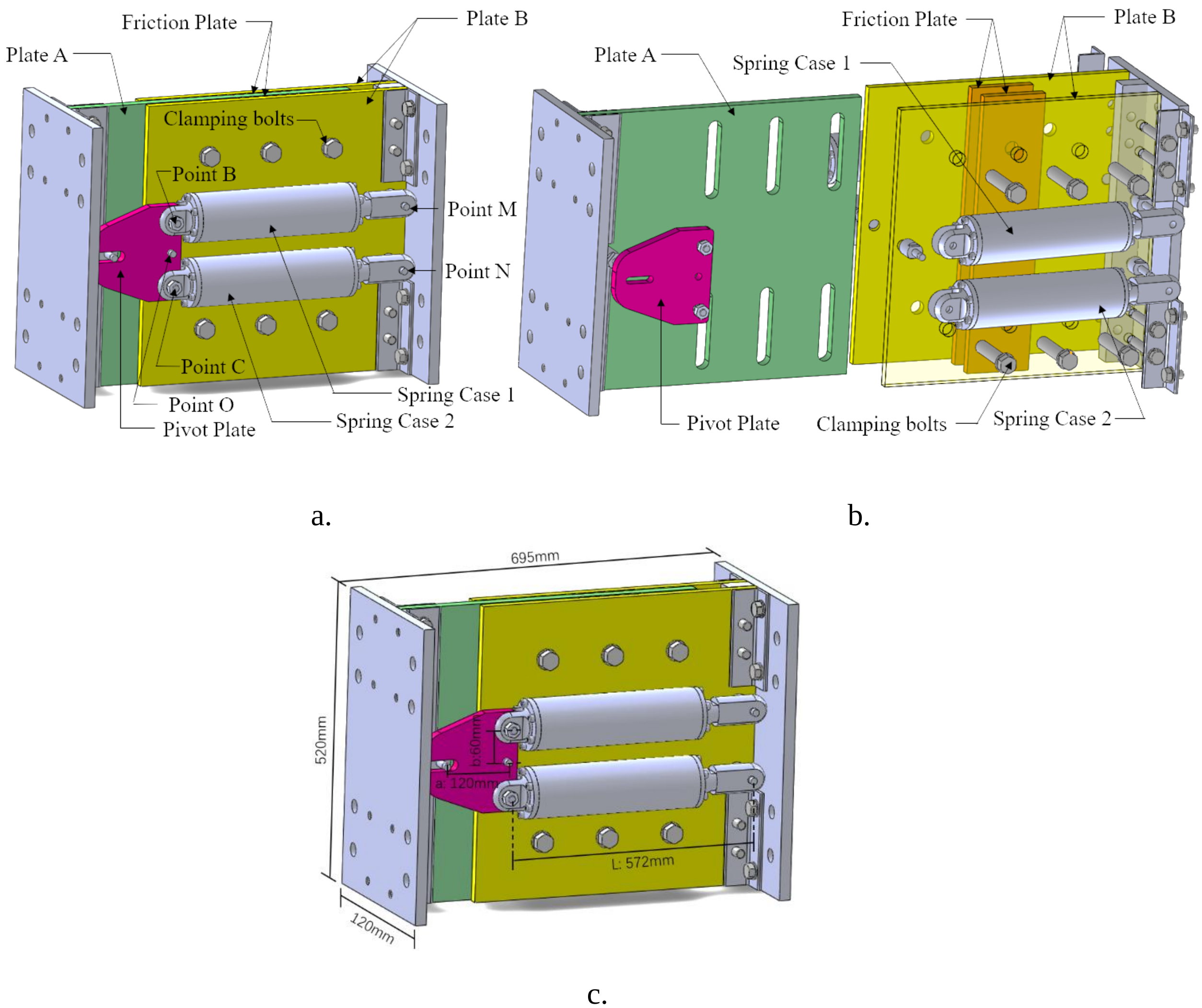

Figure 2.1 (a) Assembly view of SCNFD (b) Exploded view of SCNFD (c) Dimension of SCNFD

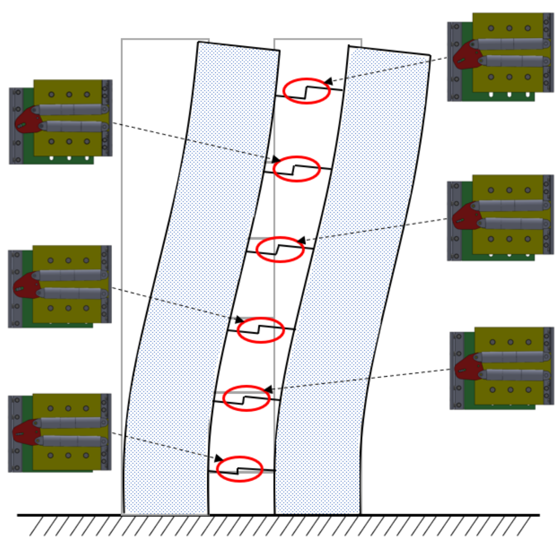

Figure 2.2 Example application of SCNFD

The SCNFD consists of 5 principle components: Plate A, Plate B, friction plate, spring case and pivot plate, as illustrated in Figure 2.1. The Plate A has slotted holes while Plate B has circular holes, thus allowing relative vertical displacements while restraining rotations. The friction plate is made of a high hardness (around 500HBW) material, such as Bisalloy 500, Hardox500 and NM500. In this research, Bisalloy 500 is used as the material of friction plate. The friction plate is sandwiched between Plate A and B using the clamping bolts. The friction plate is made of a high hardness. In this research, Bisalloy 500 was used as the material of friction plates. In addition, a pivoting plate is placed between Plate A at Location O (Figure 2.1a) and the two spring cases. While the other end of the spring cases was connected to Plate B at Location M (Spring Cases 1) and at Location N (Spring Cases 2), respectively.

Pre-compressed springs are placed inside the spring cases. As shown in Figure 2.3, the spring case is in its initial length, and the spring is pre-compressed. When the spring case is elongated, the spring will be shorten caused by the motion of the left end of the bar. And when the spring case is shortened, the spring will be shorten caused by the motion of the right end of the bar. Thus, no matter the case is elongated or shortened, the spring will always in a compressed state due to the configuration of the spring case. Hence, the SCNFD will always self-center. In addition, the clamping force on the friction plate can be easily changed if different energy dissipation behavior is expected. Besides, springs with different stiffness can be replaced inside the spring case, and the pre-compressed load can be changed by using different length of spacers. The bilinear behavior of the spring is verified through experimental tests. Figure 2.4 shows the degree of freedom (DOF) of the SCNFD. It should be note, the axial and rotation DOFs are restrained.

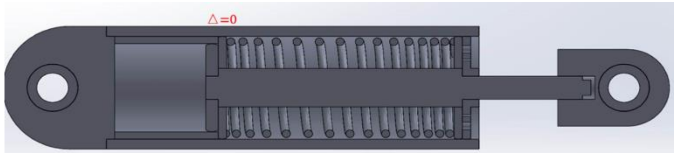

a. Initial length

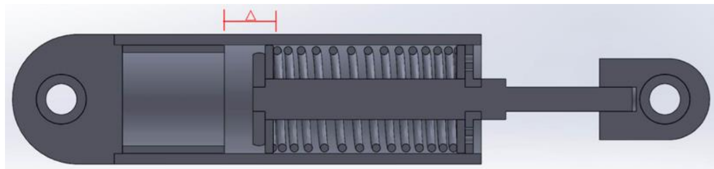

b. Elongated

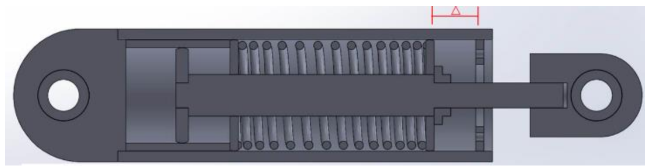

c. Shorten

Figure 2.3 Spring case

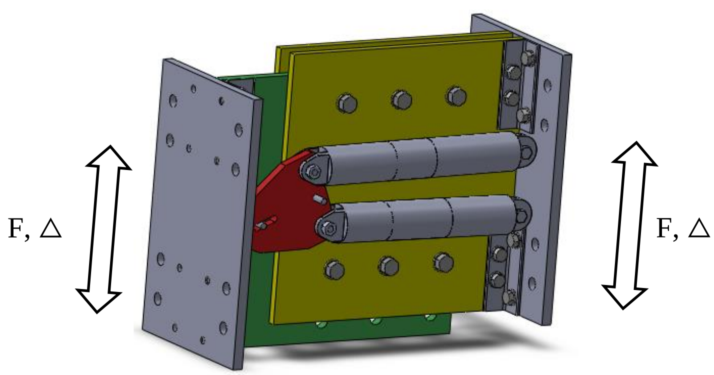

Figure 2.4 Degree of freedom of SCNFD

2.2 Hysterical behavior of the SCNFD

Figure 2.5 shows the nonlinear force-deformation response of SCNFD. Location O is always on the red dashed line, then the relative motion between Location A and O can be clearly seen in the picture. SCNFD is assumed to have rigid behavior prior to sliding. In other words, the displacement will stay at zero, while the force increases up to the sliding force, P_0. When the applied force exceeds the sliding force, P_0, the force-deformation response of the SCNFD start to follow the nonlinear curve between P_0 and P_m, where P_m is the maximum design force of SCNFD. When the displacement reverses, the force drops from P_m to P_u. The difference between P_m and P_u is the friction force generated between Plate A and the friction plate. As the deformation continues to decrease, the force-deformation response follows the nonlinear curve between P_u and P_r. The force then reverses sign when the displacement moves in the negative direction. It should be noted that the deformed configuration of the SCNFD is displacement dependent. In other words, deformed configuration of SCNFD is identical when the force is at P_m and P_u. Similarly, the deformed configuration of SCNFD is identical when the force is at $-P_\mathrm{m}$ and -P_u.

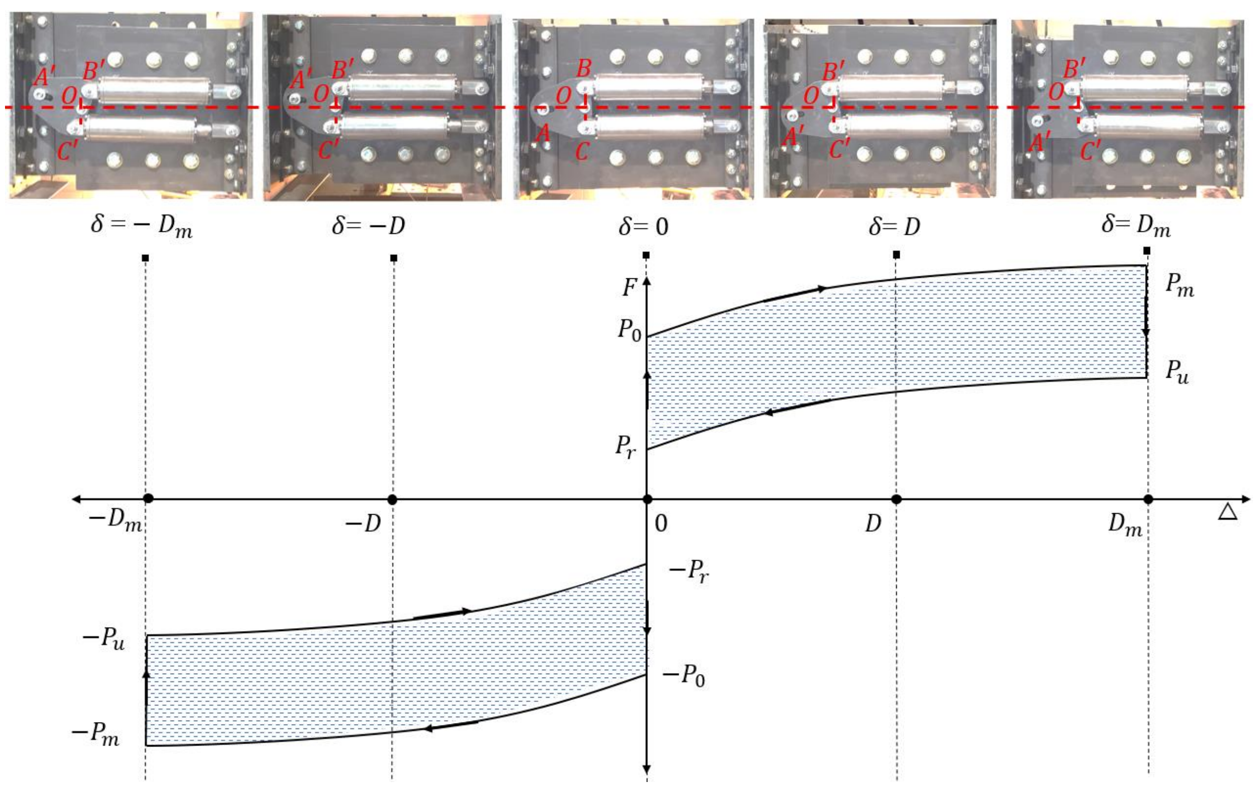

Figure 2.5 Damper motion and the corresponding hysterical behavior

2.2.1 Theoretical equations

As described in the previous session, the pivot plate is connected to Plate B at Location O, while connecting to Plate A through the slotted hole at Location A and the two spring cases at

Location B and C, respectively. As Plate B moves up, the slotted hole will force Location A to move down vertically from A to A’ (no horizontal displacement). At the same time, the pivot plate will force one end of the Spring Case 1 to move from B to B’ and Spring Case 2 from C to C’.

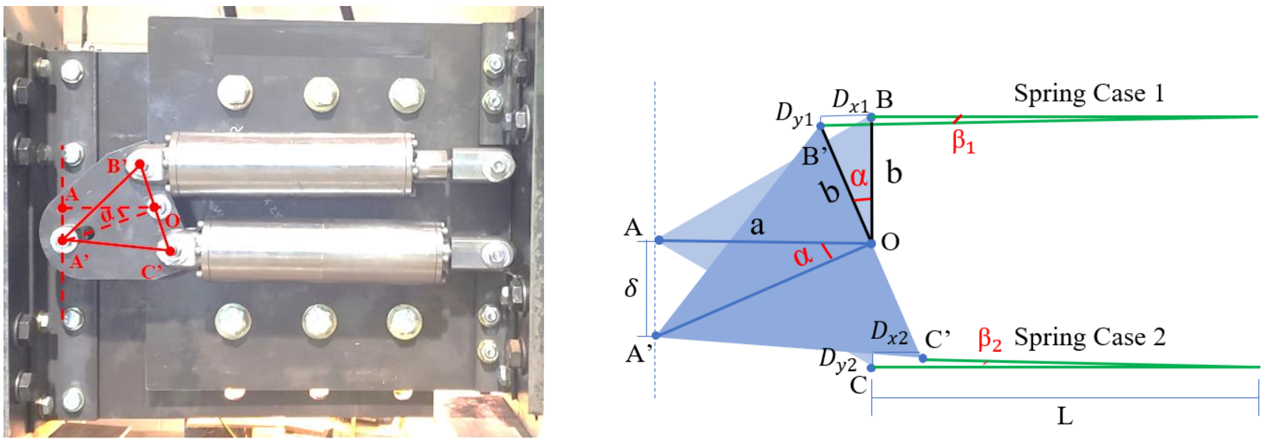

Figure 2.6 Deformed configuration of SCNFD

The design of the SCNFD assumes the length of the initial spring cases is L, the axial stiffness of the spring inside one spring case is k, the pre-compress load of each spring inside one spring case is P_c. It should be noted that, there are two pivot plates and four springs in one SCNFD. In other words, SCNFD is symmetrical between the front and back faces. Thus, the spring stiffness and pre-compressed load are double.

Using the geometry shown in Figure 2.6, the rotational angle α can be calculated using Eq. 1.

$$\alpha = \arctan\,(\delta/a) \tag{1}$$

The displacement of Location B (D_{x1}, D_{y1}) and Location C (D_{x2}, D_{y2}) are shown in Eq. 2 and Eq. 3, respectively.

$$D_{x1} = D_{x2} = b * sin\alpha \tag{2}$$

$$D_{y1} = D_{y2} = b - b * cos\alpha \tag{3}$$

The forces in the Spring Case 1 and 2 are shown in Eq. 4 and 5, respectively.

$$F_1 = 2k(\sqrt{(L + D_{x1})^2 + D_{y1}{}^2} - L) + 2P_C \tag{4}$$

$$F_2 = 2k(L - \sqrt{(L - D_{x2})^2 + D_{y2}{}^2}) + 2P_C \tag{5}$$

The rotation angles of Spring Case 1 and Spring Case 2 are shown in Eq. 6 and 7, respectively.

$$\beta_1 = \arctan\left(\frac{D_{y1}}{L+D_{x1}}\right) \tag{6}$$

$$\beta_2 = \arctan\left(\frac{D_{y2}}{L-D_{x2}}\right) \tag{7}$$

The horizontal and vertical component of F_1 and F_2 can be shown in Eq. 8 and Eq.11

$$F_{1x} = F_1 * \cos\beta_1 \tag{8}$$

$$F_{1y} = F_1 * \sin\beta_1 \tag{9}$$

$$F_{2x} = F_2 * \cos\beta_2 \tag{10}$$

$$F_{2y} = F_2 * \sin\beta_2 \tag{11}$$

Figure 2.7 shows the free body diagram of the SCNFD when the deformation is positive, where F_1, F_2 and F_1', F_2' are interaction force with each other

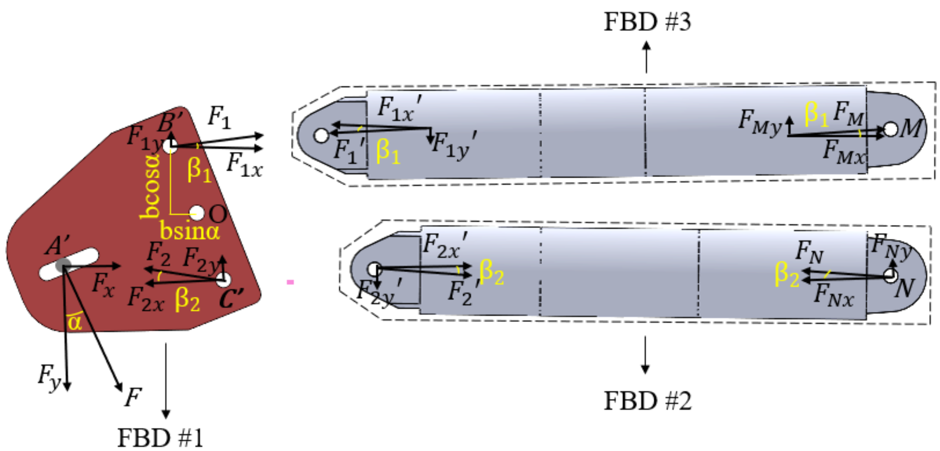

Figure 2.7 Free body diagram of the SCNFD

Because Location O is a hinge, using FBD # 1, the total moment about Location O should be zero. Hence, the force F at Location A' can be calculated using Eq. 12.

$$F = \gamma * cos\alpha(F_{1x}cos\alpha + F_{1y}sin\alpha + \; F_{2x}cos\alpha - F_{2y}sin\alpha) \tag{12}$$

where $\gamma = \frac{b}{a}$

Force in the shear direction can be calculated as Eq. 13

$$P = Fy = F{*}cos\alpha \tag{13}$$

The initial sliding force can be calculated by substituting △ = 0 into Eq. 1 and Eq. 13. Eq. 14 shows the initial force of the SCNFD.

$$P_0 = \gamma * 4P_C \tag{14}$$

2.2.2 Maximum deformation

It should be noted that the nonlinear mechanism could leads to negative stiffness if the deformation passes the maximum displacement. Figure 2.8 shows the force-deformation relationship and the post-yield stiffness relationships of SCNFD when the damper moves in positive direction. The force P is normalized using the initial sliding force P_0. The post yield stiffness k_p is normalized using the spring stiffness k. The drift ratio (△) is normalized using the vertical deformation δ divided by the length of the SCNFD (a + L). As shown in Figure 2.8a, after the shear force reaches the peak value, the negative stiffness happens. Thus, it is important to find the maximum displacement. By taking derivative of shear force P against displacement δ, the post stiffness k_p equation can be derived. Figure 2.8b shows the post stiffness deformation relationship. The maximum displacement can be obtained by setting the post stiffness $k_p$equals to zero. Close form equation for the post stiffness is shown in Appendix A.

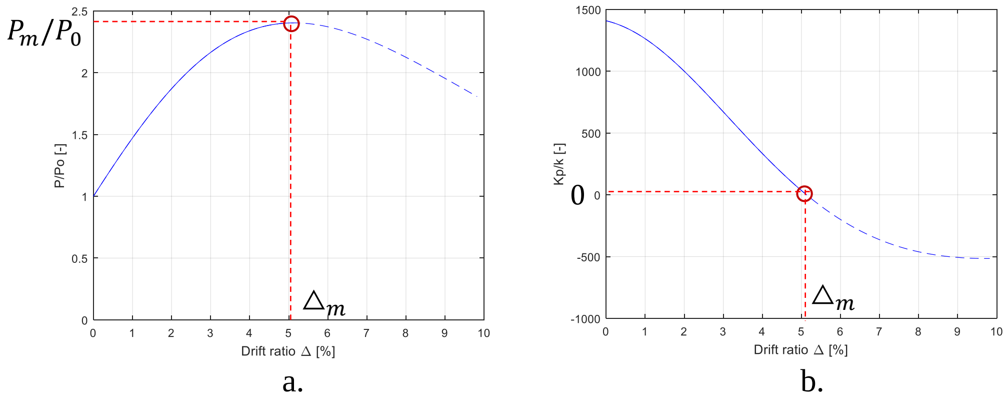

Figure 2.8 Force-deformation and stiffness-deformation relationship pf the SCNFD

Figure 2.9a shows the force deformation response of the SCNFD without the friction pad. The vertical axis is normalized using the initial presentation force P_0. The vertical deformation is normalized using the length of the SCNFD (a + L). The flag-shaped hysteretic loop (Figure 2.9c) can be regarded as the superposition of self-centering and energy dissipation capacity (Figure 2.9b). It should be noted that, the friction force F_f should be smaller than P_0. Otherwise, the damper is not self-centering (Figure 2.11).

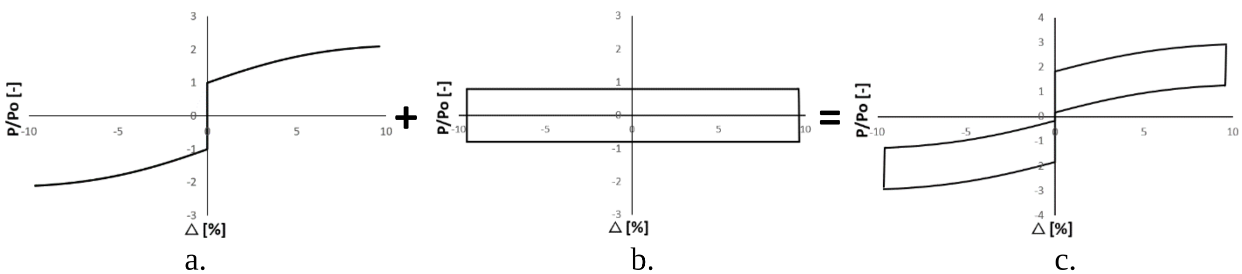

Figure 2.9 Nonlinear behavior of the pivot plate mechanism ($F_f < P_0$)

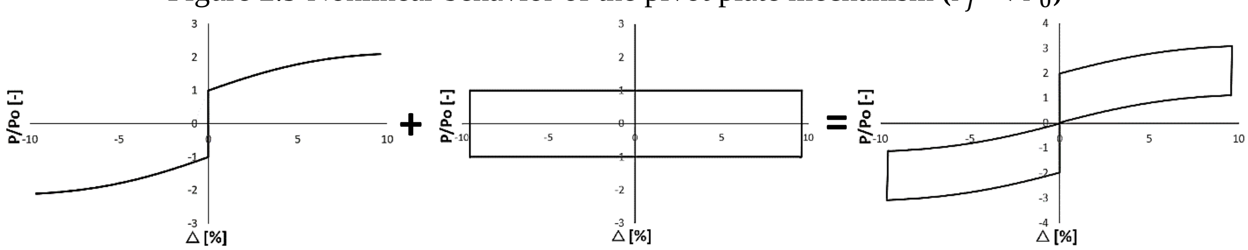

Figure 2.10 Nonlinear behavior of the pivot plate mechanism ($F_f = P_0$)

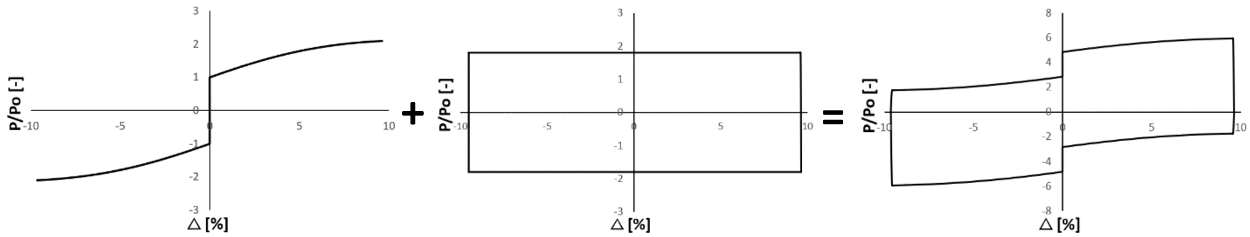

Figure 2.11 Nonlinear behavior of the pivot plate mechanism ($F_f > P_0$)

2.3 Equation verification through finite element model in Abaqus

To verify the derived equations of self-centering mechanism, a finite element model developed using ABAQUS/CAE 6.14-1 with the pivot plate and springs is conducted. Since the flag-shaped hysteresis behavior can be regarded as the superposition of self-centering and energy dissipation capacity, and the friction is a constant value. Thus, it is important to verify the backbone of the hysteresis nonlinear curve. As a result, the model consists of pivot plate and pre-compressed spring is conducted as a simplified model.

In order to achieve the verification, the motion is required to be the same as is designed; the dimensions and parameters are defined to be realistic. An overview model description, element definition, boundary condition and motion observation are presented. The comparison of the simulation results in ABAQUS and theoretical equations is shown.

2.3.1 Overview of finite element model

The finite element model designed to simulate the self-centering mechanism consists of pivot plate, bolts and spring cases. However, the convergence problem exists in the point to line contact which is used to simulate the contact between bolt and pivot plate. To solve this problem, 3D discrete rigid element is used since it is only involved in getting resultant forces instead of convergence check. Thus, the 3D discrete rigid element is adopted as the element of the bolt and 3D deformable element is adopted as the element of the pivot plate. The bilinear behavior of the spring case is simulated using the Connector element. When the spring case is elongated, the force starts from P_c and increases with the increase of axial deformation. When the spring is shortened, the force drops from $-P_c$ and continue decreases with the axial deformation increases in the direction of shortening. Both pivot plate and bolt are generated through extrusion. The material of the bolt and pivot plate is defined with Young's Modulus 2.06e5 MPa and Poisson's ratio 0.3.

Figure 2.12 shows the assembled pivot plate and bolt. The Location A, B, C and O have the same meaning as mentioned in Figure 2.1. The connection between bolt and pivot plate is defined as "frictionless hard contact"

When the damper is working, Location A moves vertically up and down, the pivot plate rotates around Location O. The horizontal distance between Location A and Location O is a fixed value, thus the bolt slides inside the slotted hole.

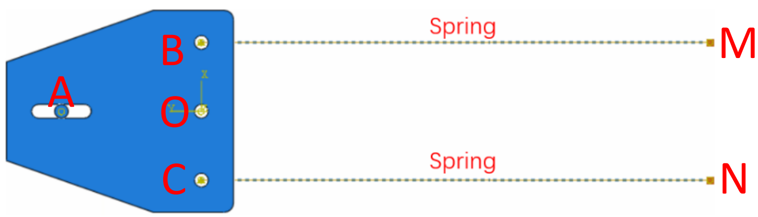

Figure 2.12 Assembled simplified SCNFD

2.3.2 Boundary conditions

The end of spring (Location M and Location N) is connected to the Plate B in real specimen, Location M and Location N will rotate when the damper is working. Thus, only rotation degree is released for Location M and Location N. The pivot plate will rotate around Location O when the bolt A is moving up and down. Location O on the pivot plate is defined to have pin boundary condition. Location B and Location C are not defined by any boundary condition. The loading reference point is on the bolt (Location A). Therefore, the loading protocol was assigned at Location A as displacement control loading in vertical direction.

2.3.3 Motion observation & equation verification

As shown in the Figure 2.13a, Location A represents the bolt inside the slotted hole. The rotate center of the pivot plate is Location O.AO and BO (CO) represent the geometric parameters a and b in the pivot plate. In this case, AO is 120mm, BO is 60mm. Location M and Location N are the end points for springs, BM and CN represents the initial length of spring cases. Location M and Location N are connected to the Plate B in the real specimen.

As shown in the Figure 2.13b, Location A moves vertically up, and the pivot plate rotates clockwise around Location O. Since the horizontal distance between Location A and Location O is a fixed value, the bolt slightly slides inside the slotted hole. Location B rotates around Location O; thus, Spring Case BM is shortened, and case CN is elongated.

As shown in the Figure.2.13c, Location A moves vertically down, and the pivot plate rotates anticlockwise around Location O. Spring Case BM is elongated, and case CN is shortened

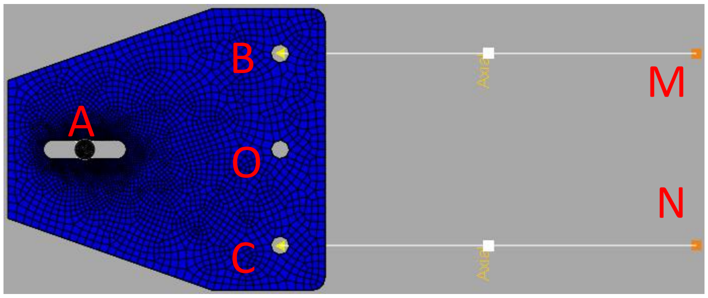

a. Initial state

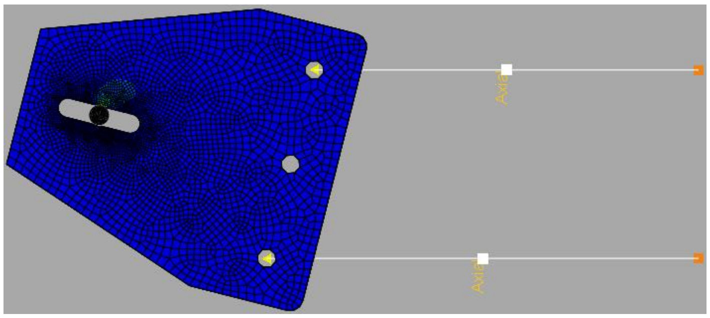
b. Location A moves up

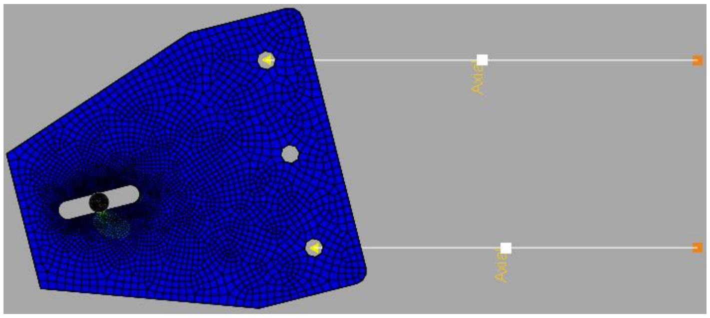

c. Location A moves up

Figure 2.13 Motion observation

The Abaqus model starts working with the Location A moves up and down. The relationship between the vertical displacement δ and shear reaction force F_{1y} is shown in the Figure 2.14. The force is normalized by the initial sliding force P_0, and the drift ratio is normalized using the vertical deformation divided by the length of the SCNFD (a+L). The comparison of theoretical equations and Abaqus model indicated the numerical result can perfectly match with the theoretical equations.

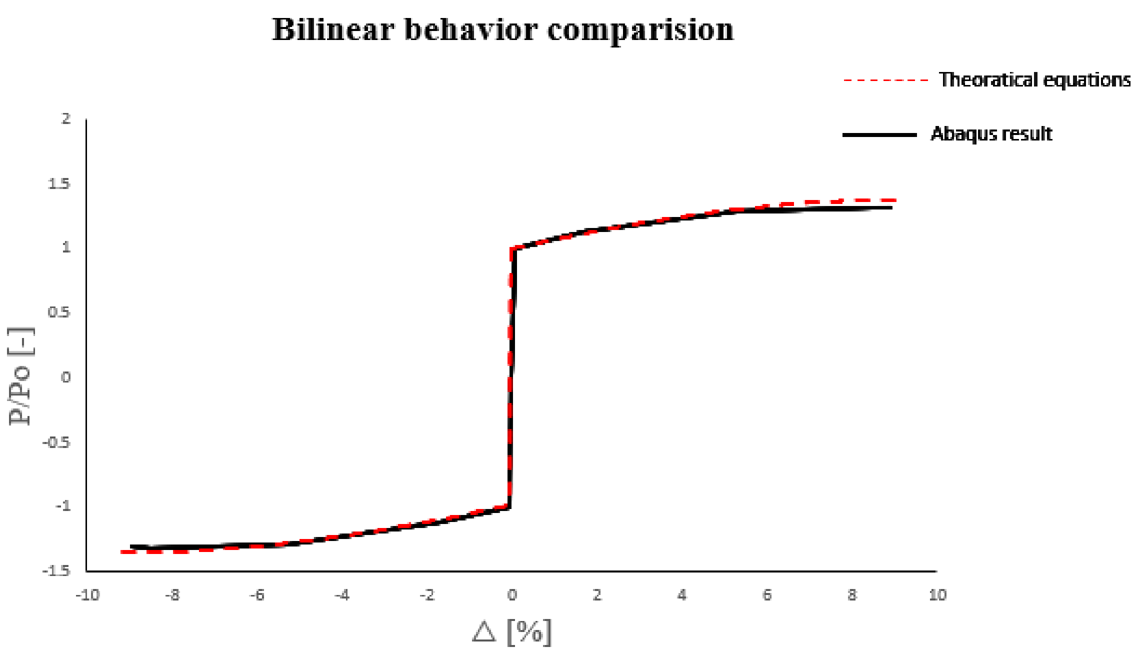

Figure 2.14 Theoratical and Abaqus results comparision

2.4 Summary

First, the concept of SCNFD is presented: using of pre-compressed spring, pivot plate and friction plates to achieve the self-centering and energy dissipated character. Then the theoretical equations are developed. Critical design parameters are discussed. Second, finite element model of the pivot plate and pre-compressed spring mechanism in the SCNFD is conducted through ABAQUS simulation. The element types, boundary conditions and motion observation are described. In the end, by comparing the simulation result with the theoretical equations, the self-centering mechanism is briefly verified.

Chapter 3: Experimental program

One prototype damper and different springs were built. The tests for the overall damper were conducted at the Structural Engineering Laboratory at the University of British Columbia, Vancouver. The main purpose of experiments is to validate the proposed flag-shaped behavior and investigate how the behavior changes as the design parameters changes. In this chapter, the test setup, components, testing matrix, instrumentation, controller and loading protocol are introduced.

3.1 Overall damper test

3.1.1 Specimen

Figure 3.1 shows the specimen tested. The height of the SCNFD is 520mm, the length is 695mm. The pivot plate dimension a equals to 120mm, b equals to 60mm. The length of the initial spring cases L equals to 572mm. The distance between two spring case is 120mm, which equals to two times b. Teflon washers were assembled to reduce friction between spring case and pivot plate. Figure 3.2 shows the front and top view of the SCNFD.

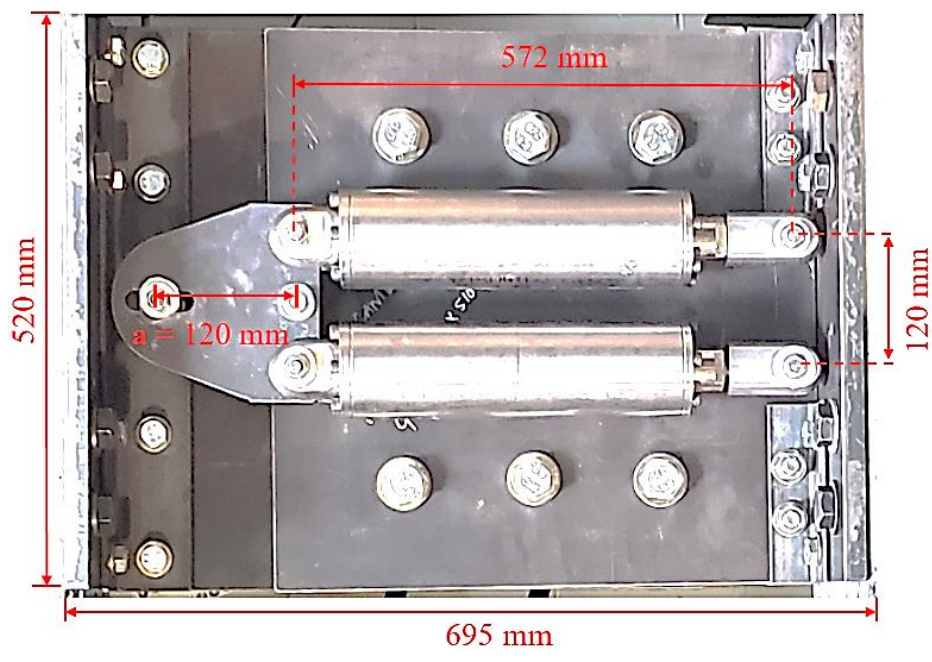

Figure 3.1 The specimen with dimensions

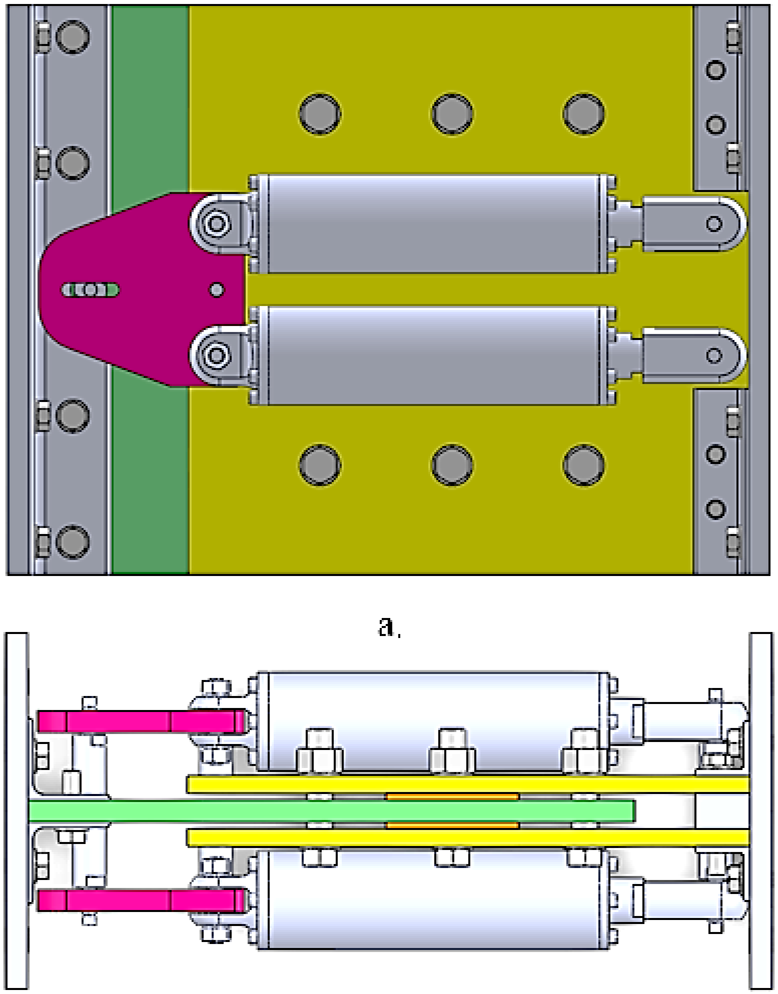

b.

Figure 3.2 a. Front view b. Top view of SCNFD

The following information show all the component detailing of the prototype.

1) Spring case

Figure 3.3 shows the key components of the spring case, which consists of shaft, spring, tube, spacer, washer and end clevis. Washers and spring are assembled along the shaft. Since Spring 1、2 and 3 have different lengths, short shaft and long shaft were used according to the lengths of springs. The length of the tube is a fixed value, a spacer is inserted inside the tube to make sure the components inside are tight and provide pre-compress length to the spring. If the shaft is short, a longer spacer should be used. The pre-compressed length of the spring is also provided washers. The washer is inserted next to the spring and placed at the end of the shaft. When the thickness of washer increases, the pre-compressed load increases. By changing the thickness of washers, the pre-compressed load can be adjusted. Grease was applied between washer and shaft to reduce friction. Besides, stainless steel was used for the fabrication of the case, which provide a smooth surface. The information of different configurations for different tests is shown in Table 3-1.

Figure 3.3 Spring case components

Table 3-1 Component configurations

Configuration	Shaft	Spacer	Washer Thickness
Spring 1 – 1.2kN Preload	Long	Short	2 x 8mm washers
Spring 1 – 2.0kN Preload	Long	Short	2 x 12.5mm washers
Spring 1 – 2.8kN Preload	Long	Short	2 x 17mm washers
Spring 2 – 1.2kN Preload	Short	Long	2 x 8mm washers
Spring 2 – 2.0kN Preload	Short	Long	2 x 11.2mm washers
Spring 3 – 1.2kN Preload	Short	Long	2 x 10.5mm washers

2) Friction Plate

Figure 3.4 shows friction plate used in this study. Based on the study presented by Golondrino (2012), Bisalloy 500 was used. The friction plate was attached to Plate A using bolts. As the relative displacement happens between Plate A and Plate B, the friction generates from the friction plate. The friction force can be changed by applying different clamping forces on bolts.

Figure 3.4 Friction plate

3) Pivot plate

As mentioned in section 2.2.1, the pivot plate transfers the vertical displacement of the SCNFD into axial deformation of the spring. There are Teflon washers at Location A, B, C and O to reduce friction.

3.1.2 Testing matrix and specimen

All components of the SCNFD are designed to be damage-free during the test. In this test, the height and length of the SCNFD is 520mm and 695mm respectively. Table 3-2 shows the design parameters of the SCNFD, where a and b are dimensions for the pivot plate, μ is the friction coefficient of the Bisalloy 500 friction plate. To reduce the friction between the pivot plate and spring case, Teflon pads were inserted. The testing matrix is presented in Table 3-3.

Table 3-2 Summary of design parameters

Parameter	Value
a	120mm
b	60mm
μ	0.21 (Hatami, MacRae et al. 2019)

Table 3-3 Testing matrix

Test	**Specimen**	**Spring stiffness [N/mm]**	**Pre-compressed load [kN]**	**Friction [kN]**
1	S88P1.2F1	87.9	1.2	1
2	S88P2.0F1	87.9	2.0	1
3	S88P2.0F2	87.9	2.0	2
4	S88P2.8F1	87.9	2.8	1
5	S88P2.8F2	87.9	2.8	2
6	S122P1.2F1	121.9	1.2	1
7	S122P2.0F1	121.9	2.0	1
8	S122P2.0F2	121.9	2.0	2
9	S186P1.2F1	185.7	1.2	1

3.2 Spring and the pre-load replacement procedure

The replacement procedure of spring and pre-load is shown in Table 3-4.

Table 3-4 Spring and the pre-load replacement procedure

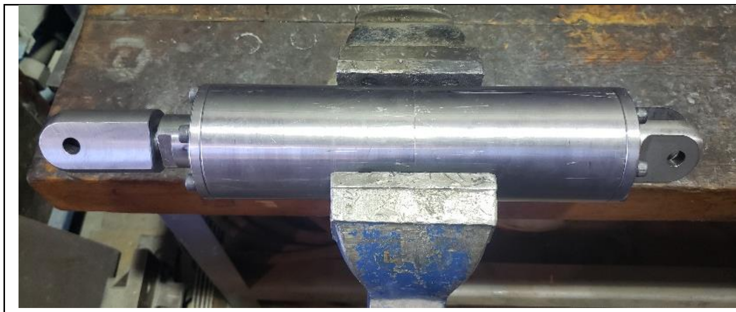	Assembled spring case
	The elements inside the spring case: washers, spring, shaft, spacer.
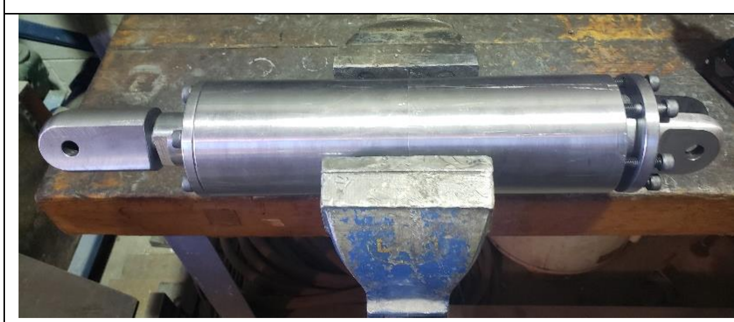	Step 1: Loose the bolt on end clevis.

	Step 2: Take off the end clevis and end screwed part
	Step 3: Take off the spacer
	Step 4: Take out the shaft together with spring and washers
	Step 5: Take off the spring and washers from the shaft

	Step 6: Since the sprsing is changed from a longer one to a shorter one, the shaft needs to be changed to a shorter one and the spacer needs to be changed to a longer one. New washers are used for new pre-compress load
	Step 7: Assemble the spring and washers to the shaft
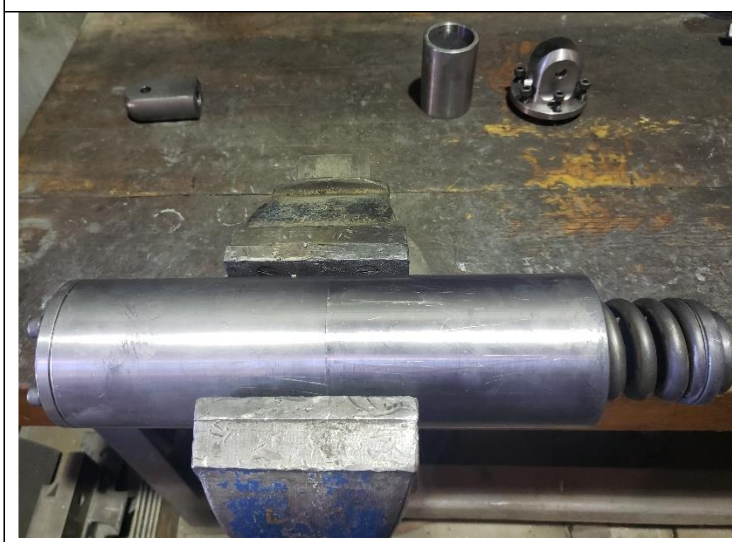	Step 8: Insert the shaft

	Step 9: Insert the spacer
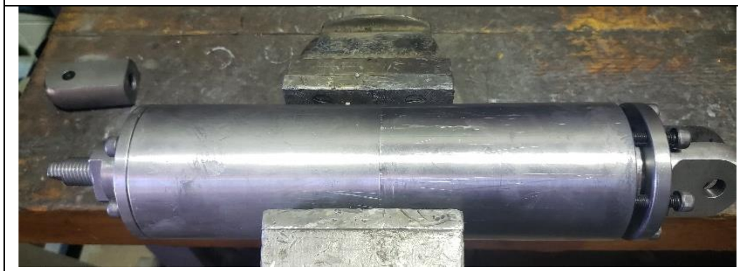	Step 10: Assemble the end clevis
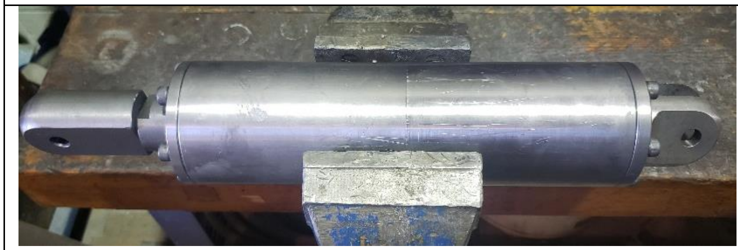	Step 11: Assemble the end screwed part

3.2.1 Experiment set up

Figure 3.5 shows the setup at the University of British Columbia used to test the SCNFD. The height and length of the setup is 2.4m and 2.9m, respectively. The setup consists of 5 main components: L-beam, pantograph, reaction frame, out-of-plane support and out-of-plane restrain. The L-beam is designed to transfer the vertical displacement from the actuator to specimen. The L-beam was fabricated using two W12x106 sections. The left side of the L-beam was inside the out-of-plane support, which can restrain the out-of-plane displacement together with the out-of-plane restrain. The right side of the L-beam was connected to the pantograph. The pantograph provides horizontal translation and avoids the rotation of L-beam. The diagonal elements were 50cm and the vertical element were 70cm. An actuator with a capacity of 1000kN and stroke limit of +/- 150mm was connected with the L-beam on the top. The specimen was connected to the L-beam and reaction frame using moment resisting bolts connections. The experimental set up was donated and fabricated by George Third and Sons, Custom Plate and Pacific Bolts. During the test, the actuator will push and pull in vertical direction.

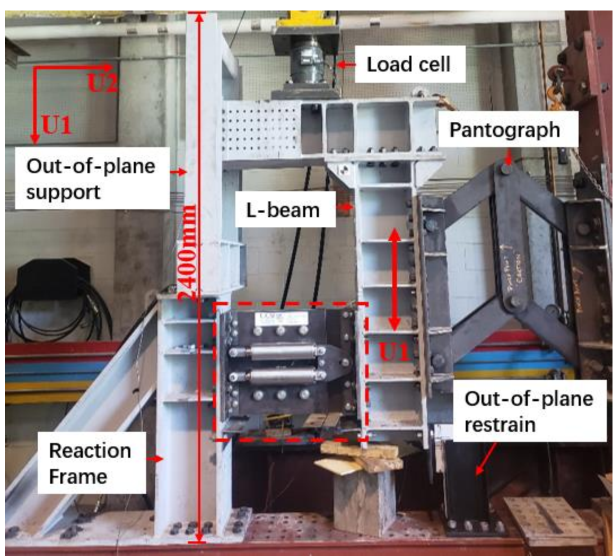

Figure 3.5 Test setup and the specimen installed

3.2.2 Loading protocol

Figure 3.6 shows the loading protocol for the test. the SCNFD is designed to be damage free, so the peak deformation is defined to be equal to the maximum drift ratio ($\triangle_m$) of SCNFD. In the test, the peak drift ratio is set as 9% by using the maximum deformation δ devided by the length of the SCNFD (a + L). There are three cycles for drift 1%, 1.5%, 2%, 3.5%, 5% and two cycles for drift 7% and drift 9%.

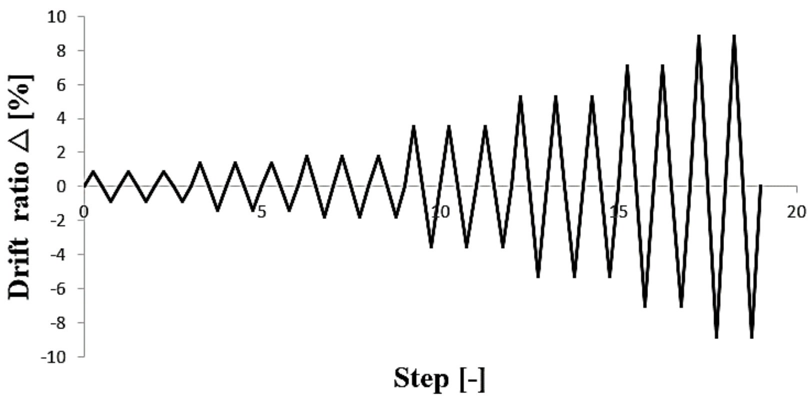

Figure 3.6 Loading protocol

3.2.3 Instrumentation

1) Load Feedback

Figure 3.7 shows the MTS 661.31 load cell used to record the load in the SCNFD. The load cell has the capacity of 1300kN. The load cell is connected between the actuator and L-beam by bolts.

Figure 3.7 Load cell

2) Displacement Feedback

The actuator has its own displacement measurement. However, the slippage cannot be avoided at all the bolt connections in the test setup. To eliminate the inaccuracy, the virtual sensor includes two linear pots (LP1 and LP2) was installed at the flanges of Plate A and Plate B. Figure 3.8 shows the setup developed.

The horizontal D_{Fx} and vertical D_{Fy}displacement of the Location F can be obtained by Eq.15 and Eq.16, respectively.

$$D_{Fx} = \sqrt{LP1^2 - \frac{(LP1')^2-(LP2')^2+L12^2}{2L12}} - \sqrt{LP1^2 - \frac{(LP1)^2-(LP2)^2+L12^2}{2L12}} \tag{15}$$

$$D_{Fy} = \frac{(LP1')^2-(LP2')^2-(LP1)^2+(LP2)^2}{2L12} \tag{16}$$

where LP1 and LP2 are the lengths of linear pots at the initial state, while LP1’ and LP2’ are lengths of linear pots at the deformed configurations.

Then the vertical displacement is collected in the virtual sensor and it is used as the displacement feedback signal to the controller.

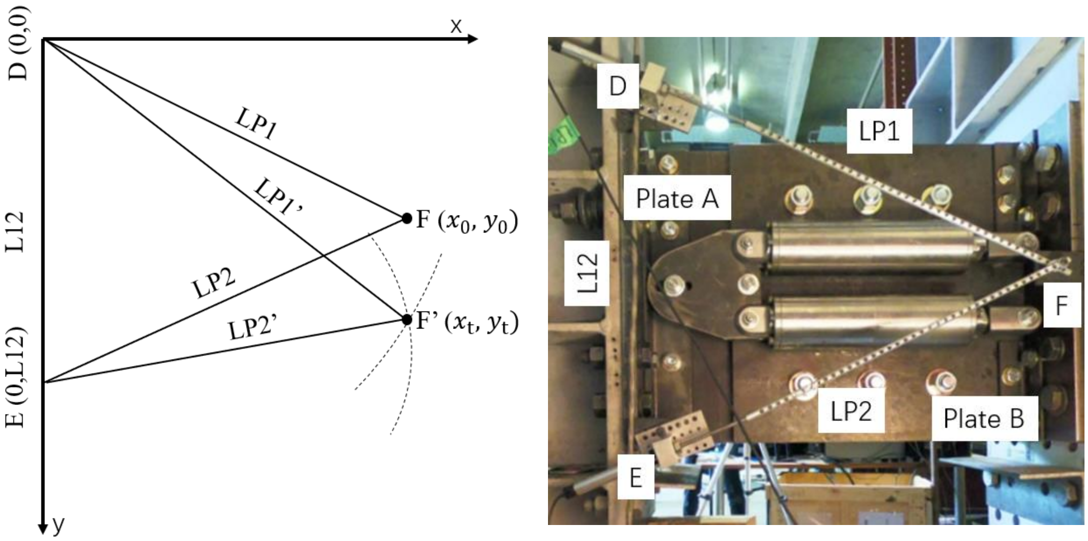

Figure 3.8 (a) Geometric relationship of virtual sensor (b) Linear pots configuration

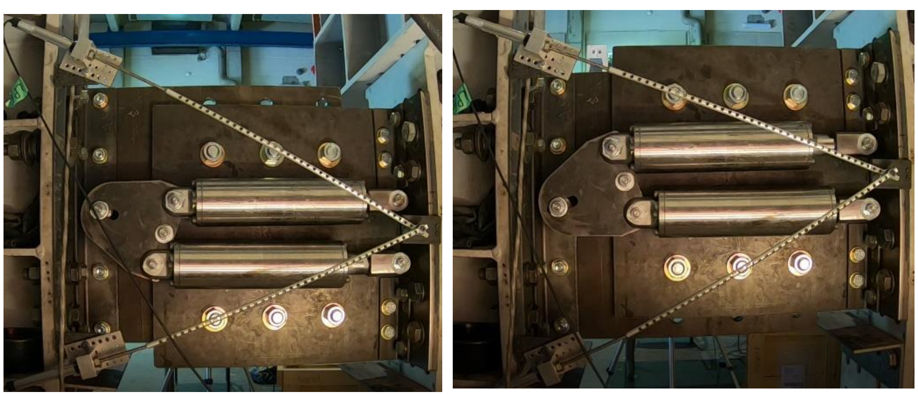
Figure 3.9 Deformed configurations of linear pots

Figure 3.9 shows the deformed configurations of linear pots. Figure 3.10 shows the horizontal and vertical displacement of Location F compared to the loading protocol. It is obvious that the vertical displacement closely matched with the loading protocol, and the horizontal displacement is almost zero. The calibration of linear pots is shown in Appendix B and the reading value of linear pots is shown in Appendix C.

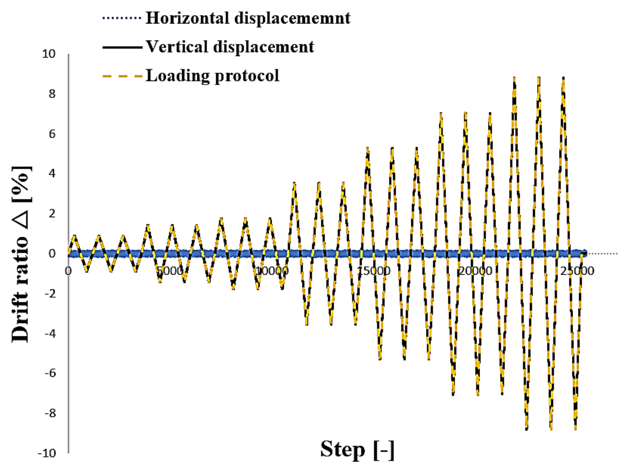

Figure 3.10 Horizontal and vertical reading value compared to loading protocol

3) Controller

Figure 3.11 ACTS controller

Figure 3.11 shows the controller used to control the test. In this study, the ACTS controller is used to control displacement demand shown in Figure 3.6. The ACTS controller has several channels, such as displacement, force and acceleration channels to control the test set up by giving the output signal to servo valve. In this test, the output signal (reference signal) is the loading protocol and the input signals are the readings of LP1, LP2 and load cell (The load cell reading is shown in Appendix D). The readings of LP1 and LP2 are converted to vertical displacement in virtual sensor (feedback signal) by dll extension file. Besides, alarms can be set to avoid unexpected damage. During the test, the ACTS provides real-time plotting to visualize all kinds of signals.

3.3 Testing procedure

Some preparation works needed to be done before each test. First, the spring and pre-compressed load should be checked to make sure if the replacement of springs or washers is needed. To facilitate the checking procedure, the information of spring and washers inside the spring case should be labeled on the spring tube. The spring and washers can be confirmed by checking the information on spring case. Second, two linear pots should be assembled at the back of the SCNFD. Finally, lubricant should be applied to the pantograph to reduce the friction forces.

3.4 Free run

Before the real test, free run procedure was conducted only with Plate A, Plate B and friction plate (Figure 3.11). At the beginning of the free run, the bolts supposed to apply clamping force on friction plates were loose. In other words, this running was conducted without any force in the specimen. This procedure aims to determine the additional load due to the friction and self-weight of the test setup. After several tests, the load readings from the loading cell were stable and consistent. This reading will be subtracted from the force reading in the real test. After that, different clamping forces were applied to the bolts and different value of friction force generated from the friction plate, and the friction was working as planned.

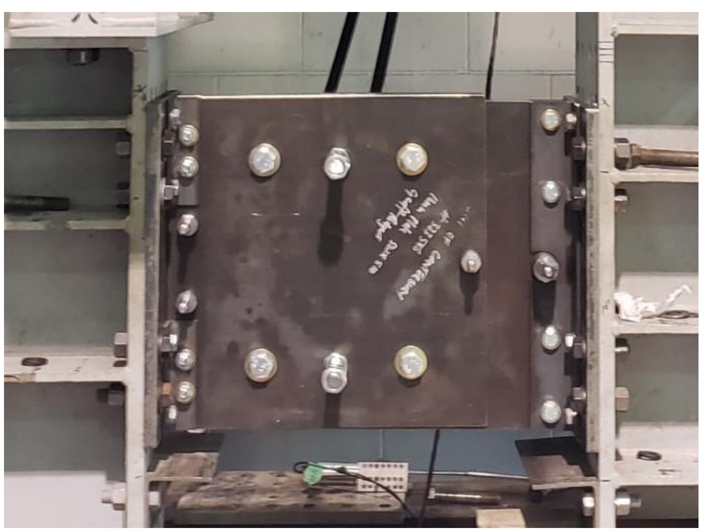

Figure 3.12 Free run

3.5 Test results

1) Free run result

As mentioned above, a free-run procedure was conducted before the cyclic test. It aims to get the additional force due to the test setup. As shown in the Figure 3.13, when the test setup moves down, the additional force is around -4.33kN. While, when the test setup moves up, the additional force has a liner relationship with the displacement. In order to get the relationship between the displacement and additional force, the fitting line is shown in Figure 3.14. This force will be later subtracted from the force reading of the load cell.

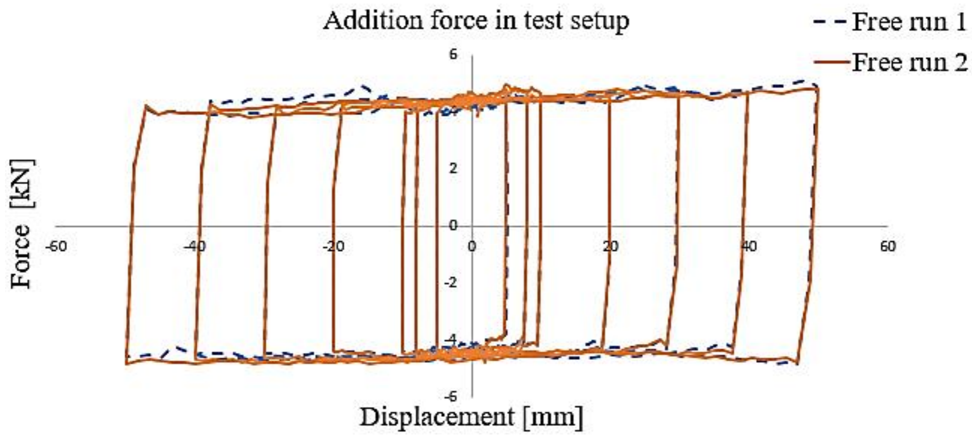

Figure 3.13 Additional force in test setup

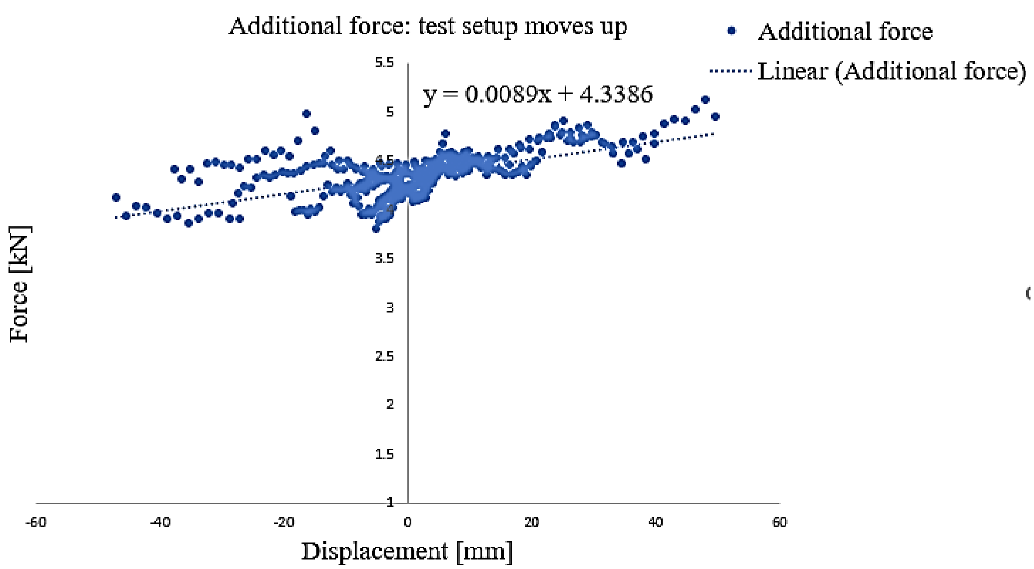

Figure 3.14 Additional force when test setup moves in positive direction

2) Cyclic result

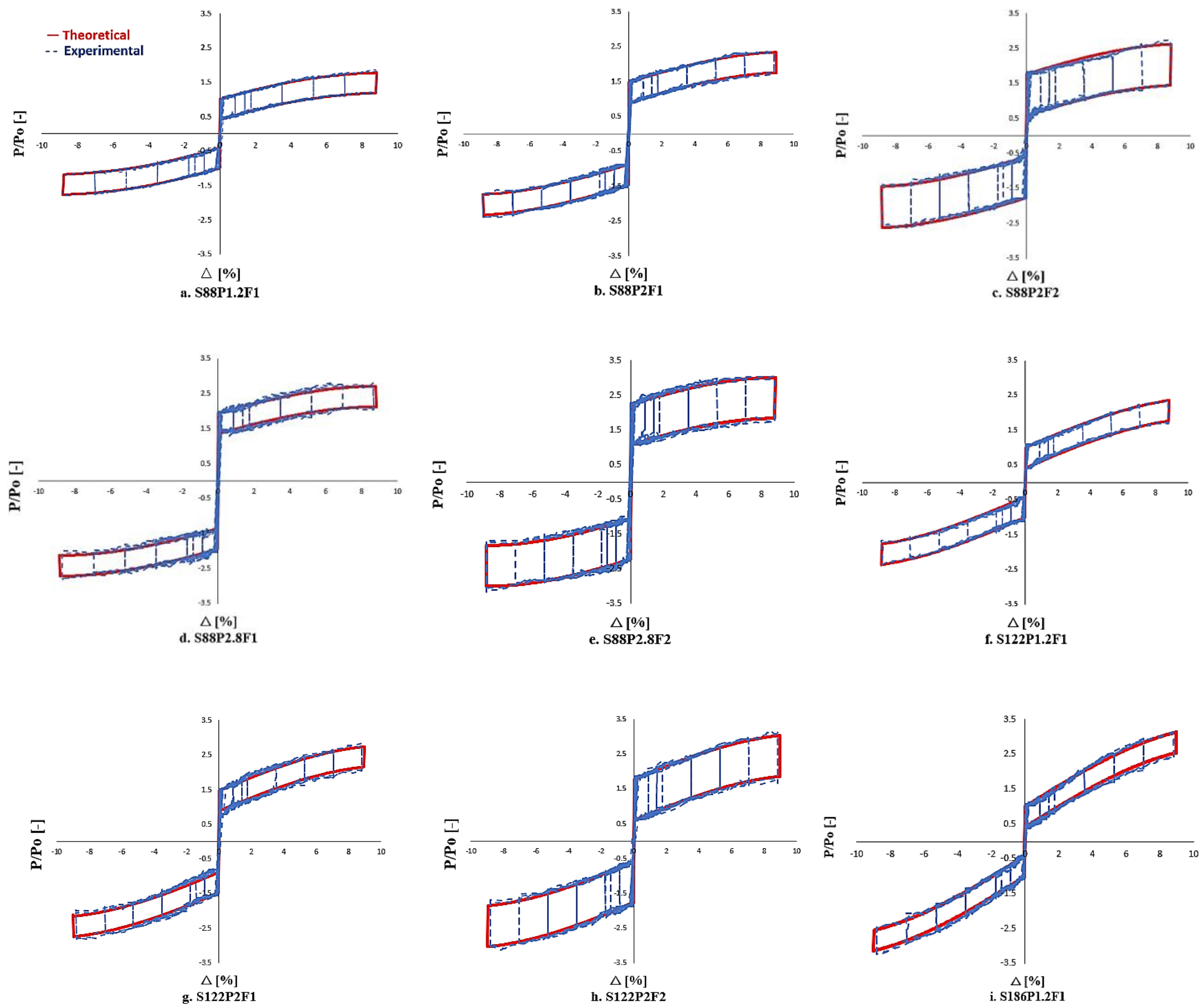

Figure 3.15 Experimental results

During the test, the SCNFD was pushed vertically to 50mm in positive direction and 50mm in opposite direction. The shear force is normalized using the initial sliding force P_0. The drift ratio (△) is normalized using the vertical deformation divided by the length of the SCNFD (a + L).

In test 1 (Figure 3.15a), specimen S88P1.2F1 has 4 springs with stiffness 88N/mm and pre-compress load 1.2kN, the friction is 1kN. It is found in the test that the initial slipping force is about 3.4kN and the maximum shear force is about 6.64kN. The post stiffness is about 64.1N/mm.

In test 2 (Figure 3.15b), specimen S88P2.0F1 has 4 springs with stiffness 88N/mm and pre-compress load 2.0kN, the friction is 1kN. It is found in the test that the initial slipping force is about 5.1kN and the maximum shear force is about 8.05kN. The post stiffness is about 59 N/mm. Compared to the result of S88P1.2F1, the initial sliding force P_0 and maximum shear force P_m in S88P2F1 increases with increasing of the pre-compress load in spring. The amount of dissipated energy is the same.

In test 3 (Figure 3.15c), the friction in specimen S88P2.0F2 is 2kN. It is found in the test that the initial slipping force is about 6.01kN and the maximum shear force is about 8.97kN. The post stiffness is about 59.2 N/mm. Compared to the result of S88P2F1, the initial sliding force P_0 and maximum shear force P_m in S88P2F1 increases with increasing of the friction load. The amount of dissipated energy in S88P2F2 increases with the increase of the friction force.

In test 4 (Figure 3.15d), specimen S88P2.8F1 has 4 springs with stiffness 88N/mm and pre-compress load 2.8kN, the friction is 1kN. It is found in the test that the initial slipping force is about 6.63kN and the maximum shear force is about 9.28kN. The post stiffness is about 53N/mm. Compared to the result of S88P2F2, the amount of dissipated energy in S88P2.8F1 decreases. The initial sliding force P_0 and maximum shear force P_m in S88P2.8F1 increases.

In test 5 (Figure 3.15e), the friction in specimen S88P2.8F2 is 2kN. It is found in the test that the initial slipping force is about 7.5kN and the maximum shear force is about 10.1kN. The post stiffness is about 52N/mm. Compared to the result of S88P2.8F1, the amount of dissipated energy in S88P2.8F2 increases. The initial sliding force P_0 and maximum shear force P_m in S88P2.8F2 increases with increasing of the friction load

In test 6 (Figure 3.15f), specimen S122P1.2F1 has 4 springs with stiffness 122N/mm and pre-compress load 1.2kN, the friction is 1kN. It is found in the test that the initial slipping force is about 3.4kN and the maximum shear force is about 8.09kN. The post stiffness is about 93.8 N/mm. Compared to the result of S88P2.8F2, the initial sliding force P_0 and maximum shear force P_m in S122P1.2F1 decreases, the amount of dissipated energy decreases. On the other hand, the post stiffness of the SCNFD increases with the spring stiffness increases.

In test 7 (Figure 3.15g), specimen S122P2.0F1 has 4 springs with stiffness 122N/mm and pre-compress load 2kN, the friction is 1kN. It is found in the test that the initial slipping force is about 5kN and the maximum shear force is about 9.3kN. The post stiffness is about 86N/mm. Compared to the result of S122P1.2F1, the initial sliding force P_0 and maximum shear force P_m in S122P2F1 increases.

In test 8 (Figure 3. 15h), the friction in specimen S122P2.0F2 is 2kN. It is found in the test that the initial slipping force is about 6.1kN and the maximum shear force is about 10.4kN. The post stiffness is about 86N/mm. Compared to the result of S122P2F1, the amount of dissipated energy increases, the initial sliding force P_0 and maximum shear force P_m in S122P2F1 increases with increasing of the friction force.

In test 9 (Figure 3. 15i), specimen S186P1.2F1 has 4 springs with stiffness 186N/mm and pre-compress load 1.2kN, the friction is 1kN. It is found in the test that the initial slipping force is about 3.3kN and the maximum shear force is about 10.5kN. The post stiffness is about 144N/mm. Compared to the result of S122P2F2, the initial sliding force P_0 in S186P1.2F1 decreases, the amount of dissipated energy decreases. On the other hand, the post stiffness of the SCNFD increases with the spring stiffness increases from 122N/mm to 186N/mm.

The movement of the SCNFD during the test is shown in Figure 3.16. It should be noted that test 1-9 all have the same deformation configuration. The difference of spring stiffness, pre-compressed load and friction force which can not be seen from outside view.

a. Loading amplitude +5 mm

b. Loading amplitude -5 mm

c. Loading amplitude +8 mm

d. Loading amplitude -8 mm

e. Loading amplitude +10 mm

f. Loading amplitude -10 mm

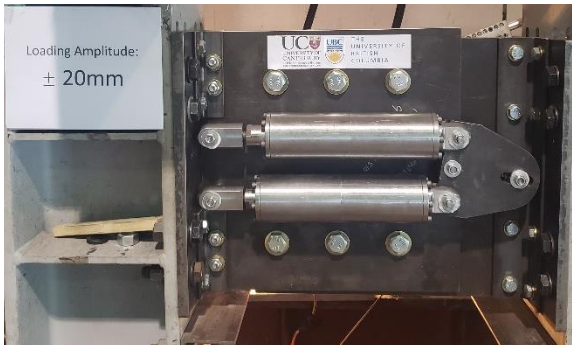

g. Loading amplitude +20 mm

h. Loading amplitude -20 mm

i. Loading amplitude +30 mm

j. Loading amplitude -30 mm

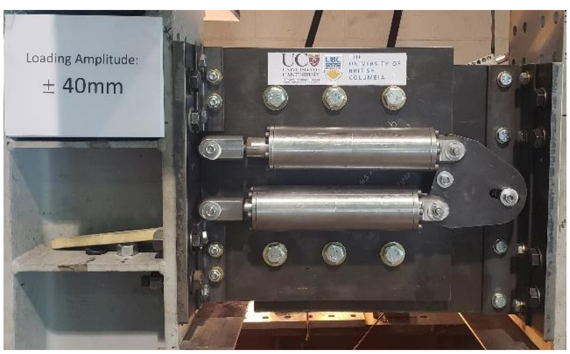

k. Loading amplitude +40 mm

l. Loading amplitude -40 mm

m. Loading amplitude +50 mm

n. Loading amplitude -50 mm

Figure 3.16 Damper movement

In general, when the stiffness (k) of the spring increase (Figure 3.15a to Figure 3.15f and Figure 3.15i), the post stiffness (kp) of the SCNFD increases. As the pre-compressed load (P_C) increases (Figure 3. 15a to Figure 3. 15b and Figure 3. 15d), the initial sliding force (P_0) increases. With the friction increases, the amount of dissipated energy increases. When it comes to the energy dissipation capacity, the increasement of friction force leads to more energy dissipation capacity. Above figures also provide the comparison between experimental results and predicted hysteresis loop. It demonstrates that the hysteresis behavior of the SCNFD is well predicted by theoretical equations. To conclude, the mechanism is verified by test and theoretical calculations, thus it can be used to conduct further parameter study.

3.6 Summary

This chapter presents the overall experimental test of SCNFD. In the overall damper test, detailed information for test setup, specimen, testing matrix and instrumentation are discussed. The free-run procedure is mentioned to determine the additional load in the test setup. Then, the results show the comparison between the prediction of the theoretical equations and experimental test. It indicates that the theoretical equations can predict the nonlinear behavior well.

Chapter 4: Parameter study

The self-centering and energy dissipation feature of the SCNFD has been verified by experimental tests. Proposed theoretical equations were also verified according to the test results. Detailed parameter study using theoretical equations was conducted to fully understand how the nonlinear hysteresis behavior varies with different parameters, which can facilitate the design procedure in the future.

4.1 Parameter study

The nonlinear elastic force-deformation response shows the post stiffness (kp) of the SCNFD decrease with the drift ratio increase. The maximum drift ratio ($\triangle_m$) is defined when the post stiffness (kp) equals to zero to avoid negative stiffness in the damper. The post stiffness of the damper (kp), the maximum drift ratio ($\triangle_m$) and the initial sliding force P_0 are important values which determine the backbone of the hysteresis loop. The initial sliding force P_0 can be obtained using Eq. (14). The post stiffness (kp) and maximum drift ratio ($\triangle_m$) are related to spring stiffness (k), pre-compressed load (P_C), the initial length of the spring case (L), and pivot plate dimension a, b. In this study, the spring stiffness (k) is selected as 80 N/mm, 120N/mm, 160N/mm and 200N/mm, the pre-compressed load (P_C) is selected as 1000N, 2000N and 3000N, the initial length of the spring case (L) is selected as 300mm, 400mm and 500mm, the dimension a and b are selected as 50mm, 150mm and 250mm. The range of those selected values are based on the practical engineering. Over 300 combinations of those parameters were studied to investigate the nonlinear behavior of the SCNFD.

4.1.1 Relationship of L and δ_m

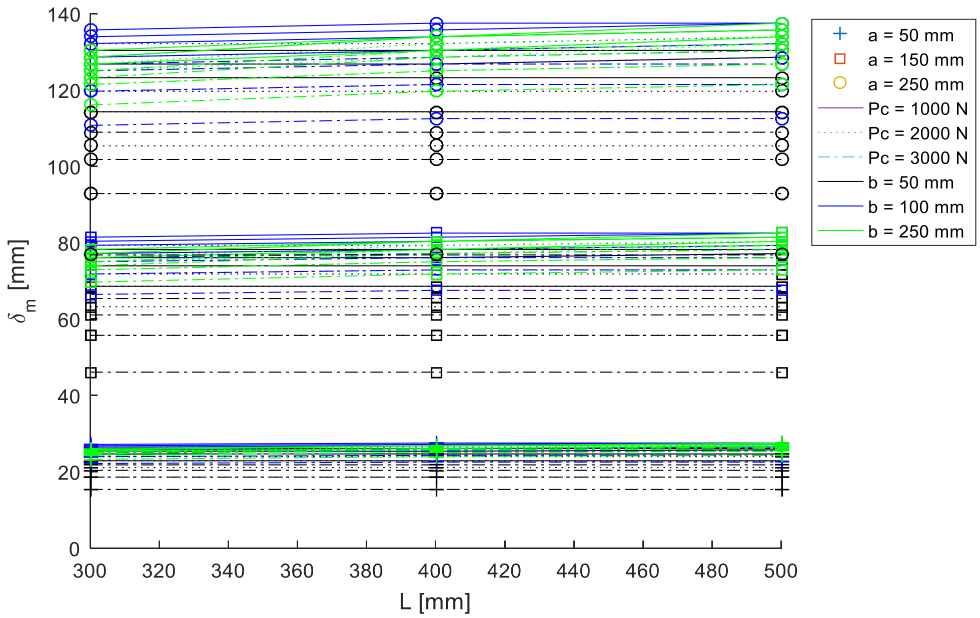

Figure 4.1 Relationship of L and δ_m

Figure 4.1 shows the influence of the pivot plate dimension a and b, pre-compressed load (P_C), the initial length of the spring case (L) on maximum displacement (δ_m). With the increase of a and b, the maximum displacement (δ_m) increases. When the L increases from 300mm to 500mm, the maximum displacement (δ_m) doesn't change much. Thus, the maximum displacement (δ_m) is independent of the initial length of the spring case (L). On the other hand, as the pre-compressed load (P_C) increases, the maximum displacement (δ_m) is more spread.

4.1.2 Relationship of P_C and $\triangle_m$

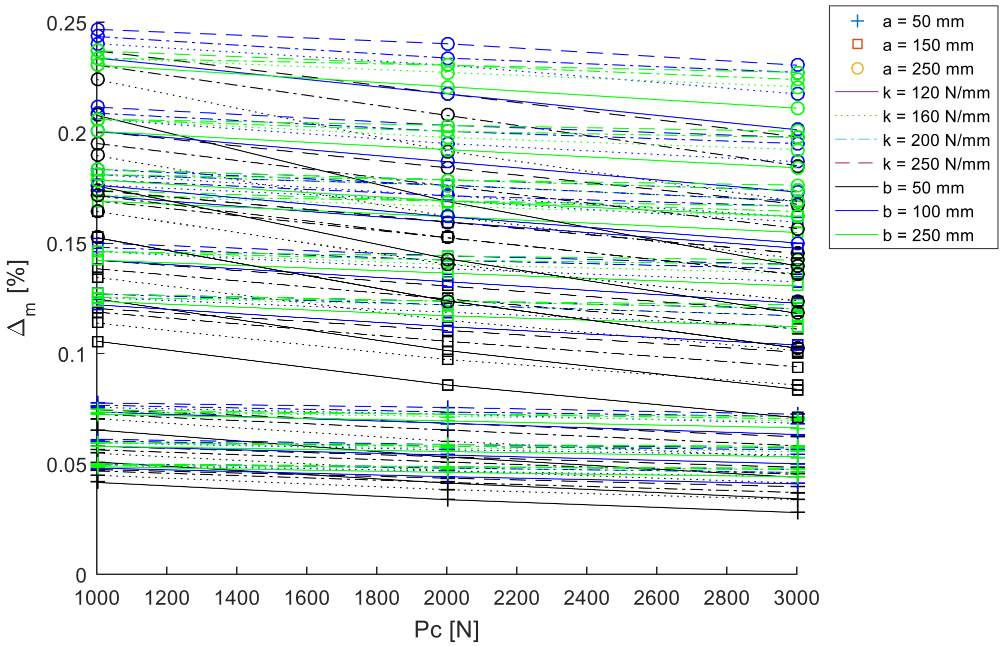

Figure 4.2 Relationship of P_C and $\triangle_m$

Figure 4.2 shows the influence of the pivot plate dimension a and b, pre-compressed load (P_C), the spring stiffness (k) on maximum drift ratio ($\triangle_m$). With the increase of a and b, the maximum drift ratio ($\triangle_m$) increases. When the pre-compressed load (P_C) increases from 1000kN to 3000kN, there is minor reduction in the maximum drift ratio ($\triangle_m$). On the other hand, as the spring stiffness (k) increases, the maximum drift ratio ($\triangle_m$) increases.

4.1.3 Relationship of k and $\triangle_m$

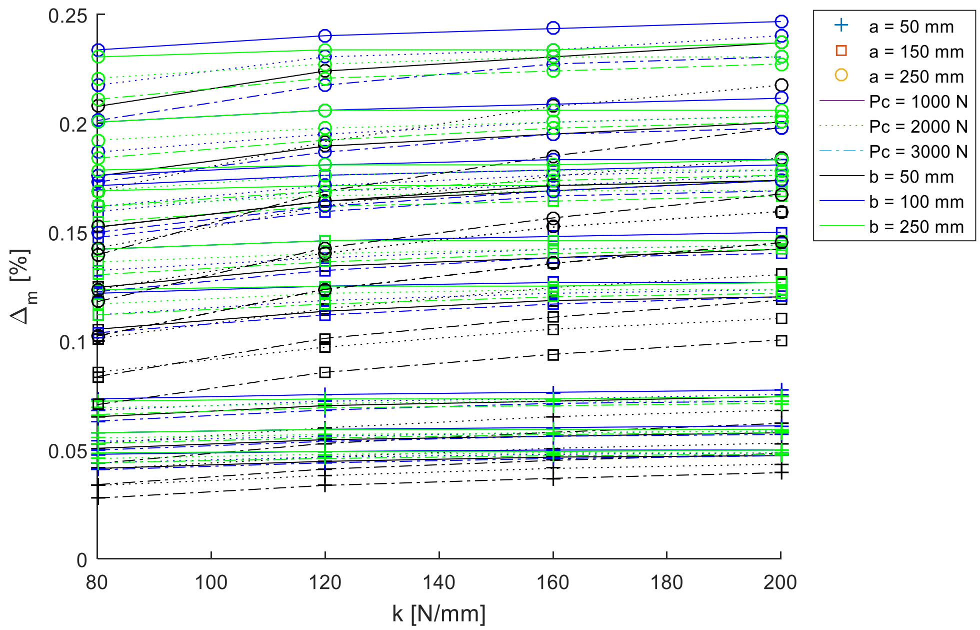

Figure 4.3 Relationship of k and $\triangle_m$

Figure 4.3 shows the influence of the pivot plate dimension a and b, pre-compressed load (P_C), the spring stiffness (k) on maximum drift ratio (δ_m). With the increase of a and b, the maximum drift ratio (δ_m) increases. When the spring stiffness (k) increases, the maximum drift ratio (δ_m) increases a little. The relationship between the pre-compressed load (P_C) and maximum drift ratio (δ_m) is not clear in this figure.

4.1.4 Relationship of a and $\triangle_m$

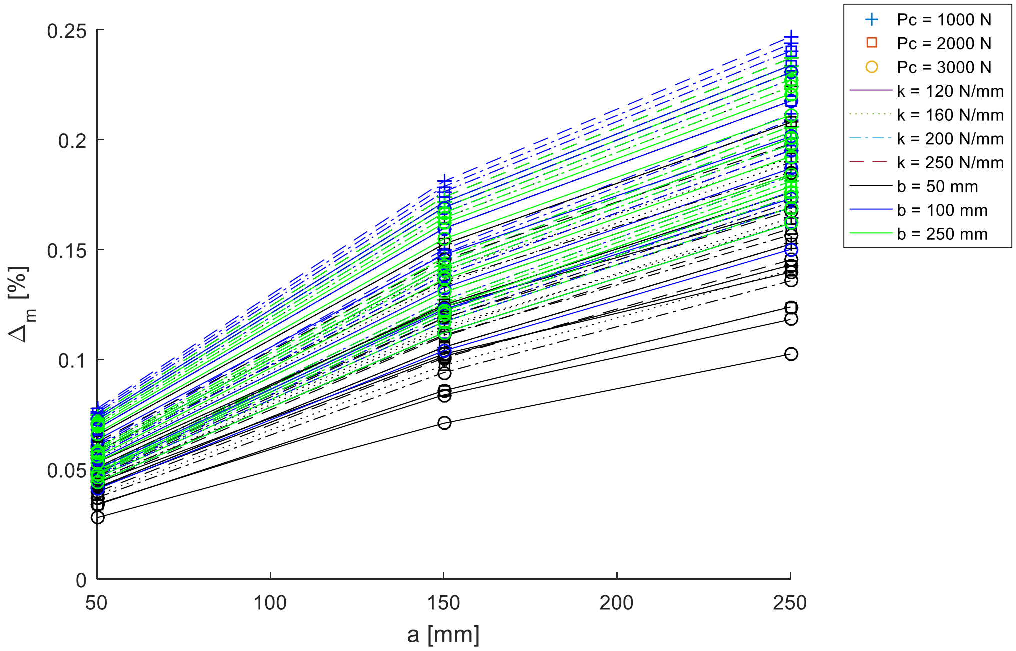

Figure 4.4 Relationship of a and $\triangle_m$

Figure 4.4 shows the influence of the pivot plate dimension a and b, pre-compressed load (P_C), the spring stiffness (k) on maximum drift ratio (δ_m). With the increase of a and b, the maximum drift ratio (δ_m) increases. When the spring stiffness (k) increases, the maximum drift ratio (δ_m) increases. Besides, the maximum drift ratio (δ_m) decreases with the pre-compressed load (P_C) increases.

4.1.5 Relationship of b and $\triangle_m$

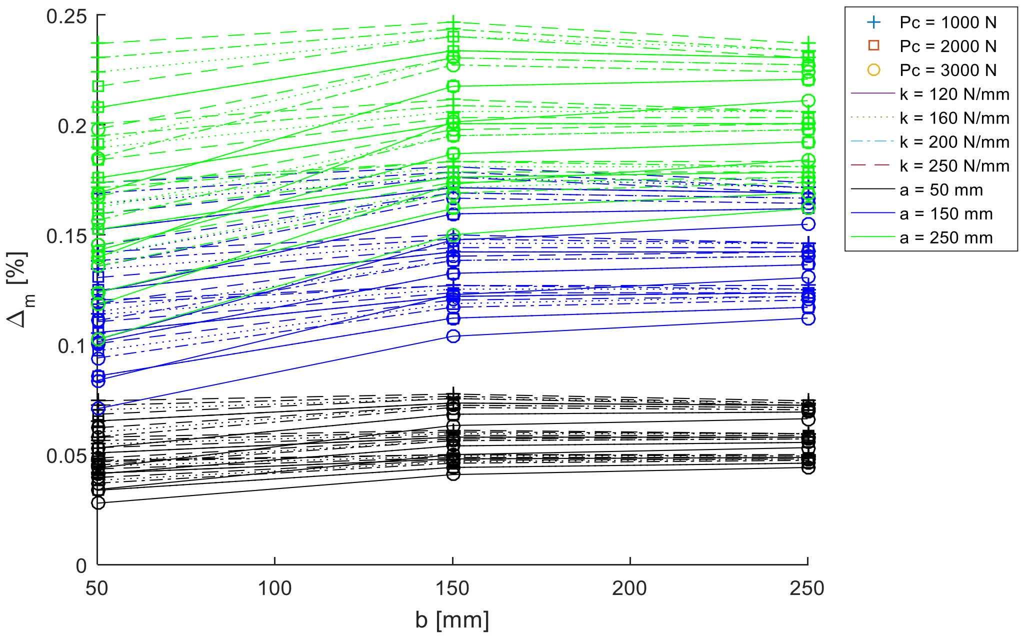

Figure 4.5 Relationship of b and $\triangle_m$

Figure 4.5 shows the influence of the pivot plate dimension a and b, pre-compressed load (P_C), the spring stiffness (k) on maximum drift ratio (δ_m). With the increase of a and b, the maximum drift ratio (δ_m) increases. The maximum drift ratio (δ_m) increases with the spring stiffness (k) increases and pre-compressed load (P_C) decreases.

Overall, the maximum drift ratio (δ_m) increases with the pivot dimension a and b, the spring stiffness (k) increase. The maximum drift ratio (δ_m) decreases with the pre-compressed load (P_C) increases.

4.1.6 Relationship of L and k_p

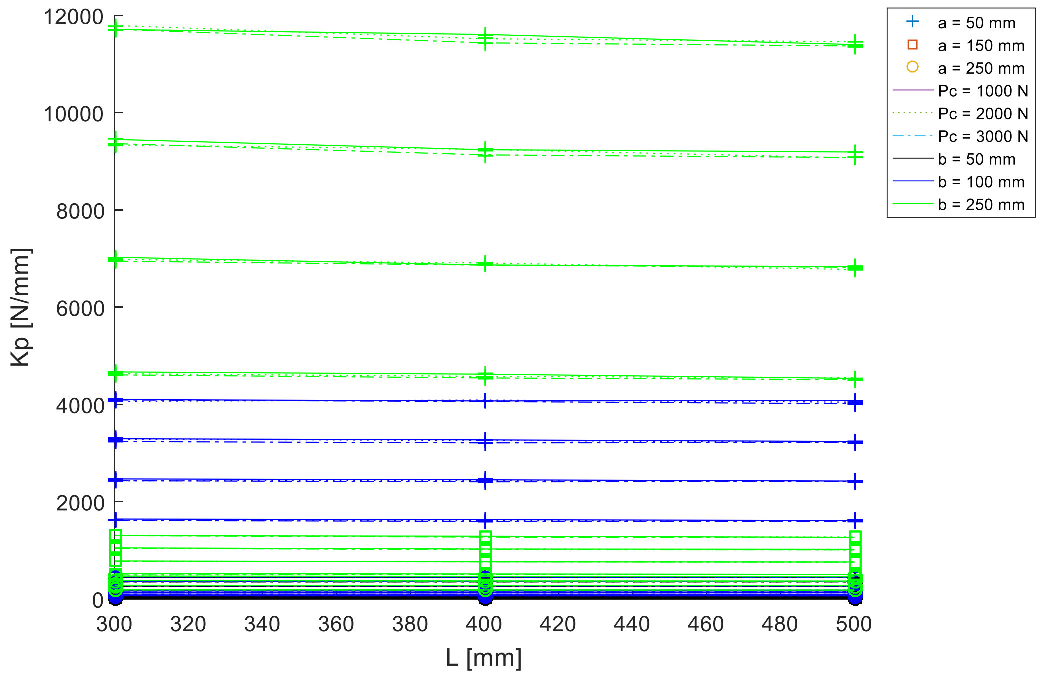

Figure 4.6 Relationship of L and k_p

Figure 4.6 shows the influence of the pivot plate dimension a and b, the initial length of the spring case (L), the pre-compressed load (P_C), the spring stiffness (k) on the post stiffness (kp). With the increase of a, the post stiffness (kp) decreases. With the increase of b, the post stiffness (kp) increases. The pre-compressed load (P_C) doesn't have much effect on the post stiffness (kp). On the other hand, when the initial length of the spring case (L) increases from 300mm to 500mm, the post stiffness (kp) doesn't change. In other words, the post stiffness (kp) is not related to the initial length of the spring case (L).

4.1.7 Relationship of P_C and k_p

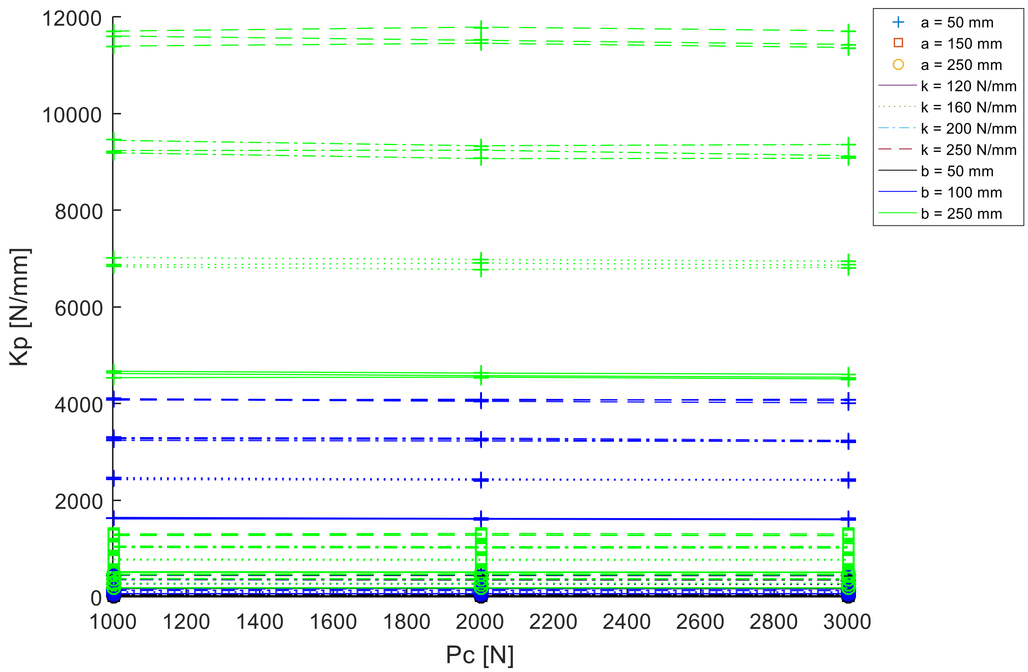

Figure 4.7 Relationship of P_C and k_p

Figure 4.7 shows the influence of the pivot plate dimension a and b, the pre-compressed load (P_C), the spring stiffness (k) on the post stiffness (kp). With the increase of a, the post stiffness (kp) decreases. With the increase of b, the post stiffness (kp) increases. Also, the post stiffness (kp) increases with the increases of the spring stiffness (k). The pre-compressed load (P_C) has minor effect on the post stiffness (kp).

4.1.8 Relationship of k and k_p

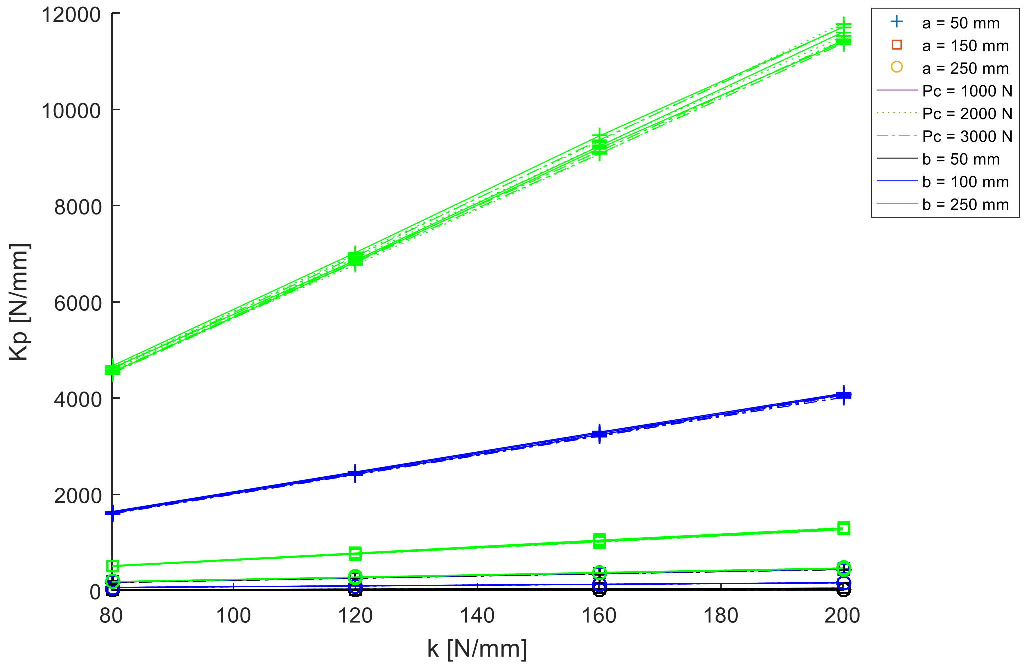

Figure 4.8 Relationship of k and k_p

Figure 4.8 shows the influence of the pivot plate dimension a and b, the pre-compressed load (P_C), the spring stiffness (k) on the post stiffness (kp). With the increase of a, the post stiffness (kp) decreases. With the increase of b, the post stiffness (kp) increases. The post stiffness (kp) increases with the spring stiffness (k) increases. The changes of the post stiffness (kp) caused by the pre-compressed load (P_C) is ignorable.

4.1.9 Relationship of a and k_p

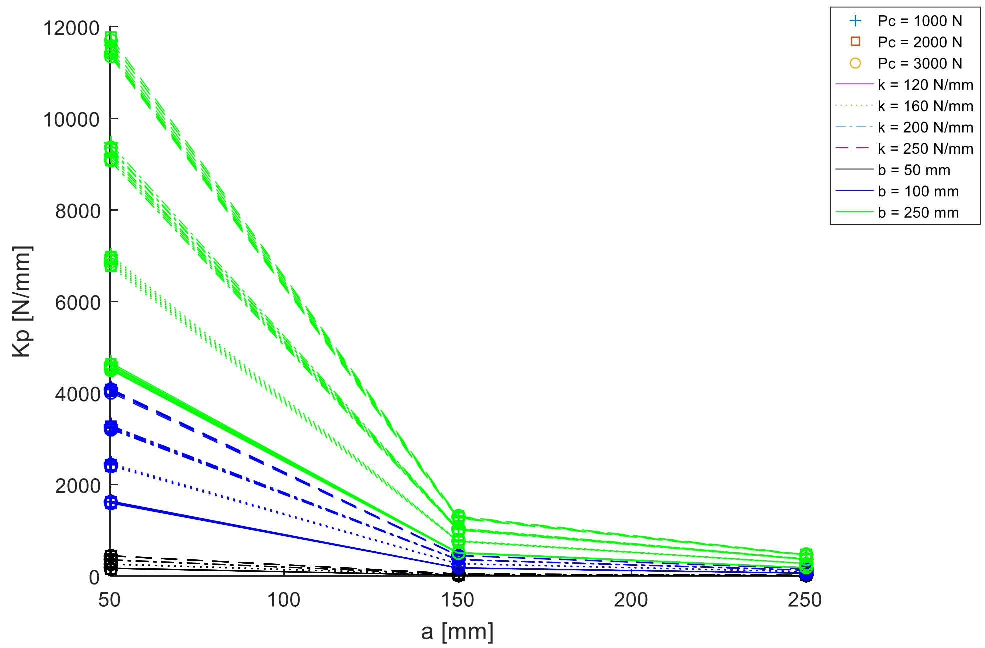

Figure 4.9 Relationship of a and k_p

Figure 4.9 shows the influence of the pivot plate dimension a and b, the pre-compressed load (P_C), the spring stiffness (k) on the post stiffness (kp). With the increase of a, the post stiffness (kp) decreases. With the increase of b, the post stiffness (kp) increases. The post stiffness (kp) also increases with the spring stiffness (k) increases. The changes of the post stiffness (kp) caused by the pre-compressed load (P_C) is ignorable.

4.1.10 Relationship of b and k_p

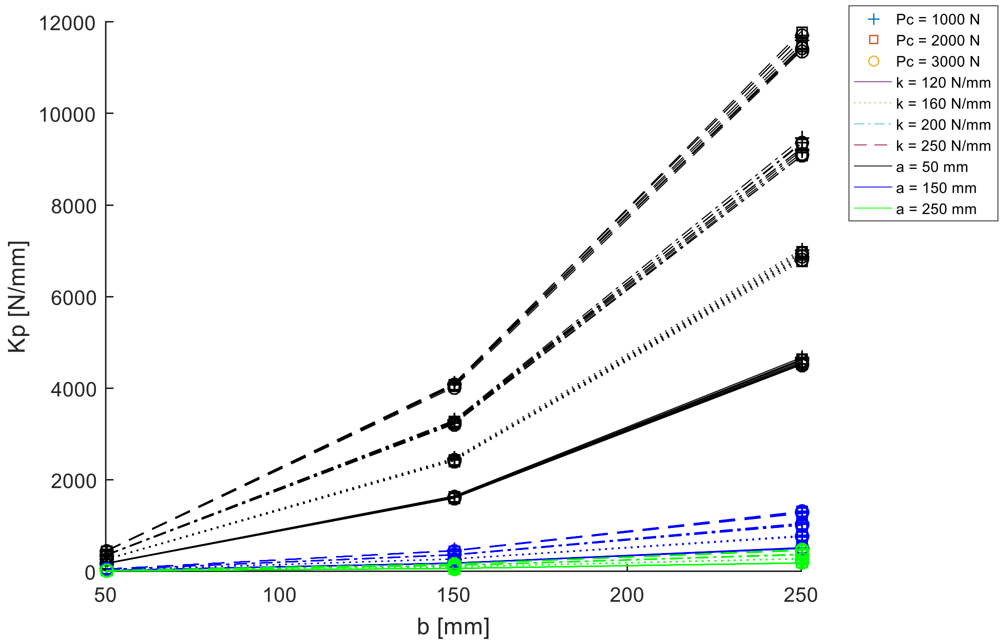

Figure 4.10 Relationship of b and k_p

Figure 4.10 shows the influence of the pivot plate dimension a and b, the pre-compressed load (P_C), the spring stiffness (k) on the post stiffness (kp). With the increase of a, the post stiffness (kp) decreases. With the increase of b, the post stiffness (kp) increases. The post stiffness (kp) also increases with the spring stiffness (k) increases.

Overall, the post stiffness (kp) increases with the pivot dimension b and the spring stiffness (k) increase. The post stiffness (kp) decreases with a increases.

4.1.11 Relationship of L and P_m/P_0

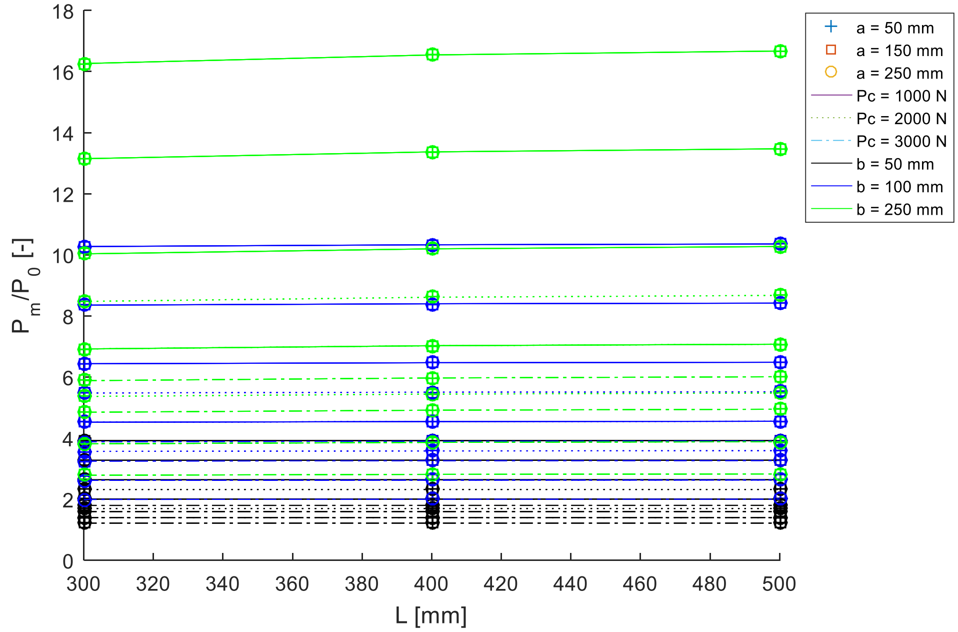

Figure 4.11 Relationship of L and P_m/P_0

Figure 4.11 shows the influence of the initial length of the spring case (L), the pivot plate dimension b and the pre-compressed load (P_C) on the normalized maximum shear force (P_m/P_0). When the L increases from 300mm to 500mm, the normalized maximum shear force (P_m/P_0) doesn’t change much. Thus, the normalized maximum shear force (P_m/P_0) is independent of the initial length of the spring case (L). With the increase of the pivot plate dimension b, the normalized maximum shear force (P_m/P_0) increases. With the increase of the pre-compressed load (P_C), the normalized maximum shear force (P_m/P_0) decreases.

4.1.12 Relationship of P_C and P_m/P_0

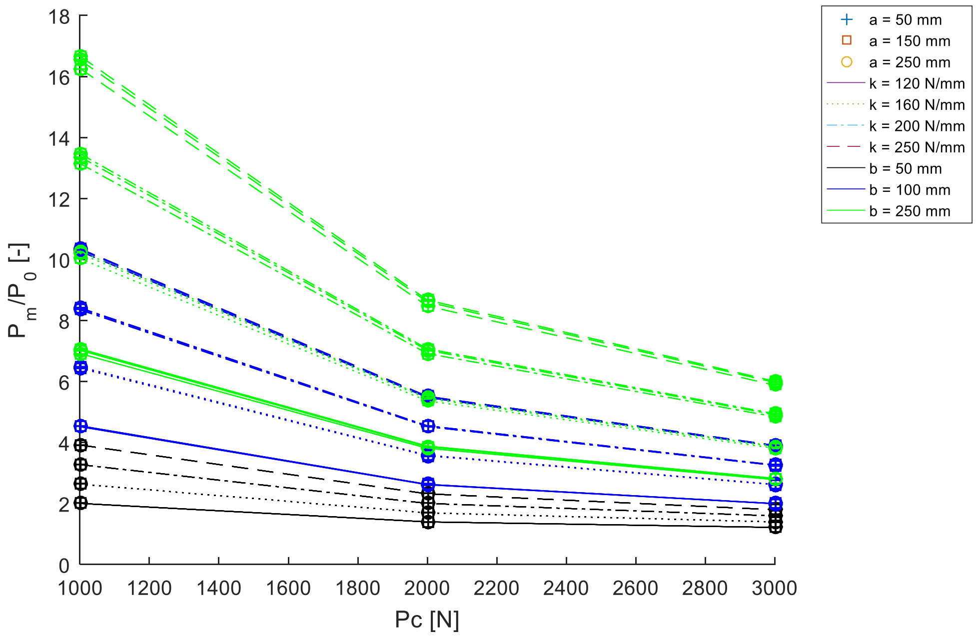

Figure 4.12 Relationship of P_C and P_m/P_0

Figure 4.12 shows the influence of the pivot plate dimension b, the pre-compressed load (P_C) and the spring stiffness (k) on the normalized maximum shear force (P_m/P_0). With the increase of the pivot plate dimension b and spring stiffness (k), the normalized maximum shear force (P_m/P_0) increases. With the increase of the pre-compressed load (P_C), the normalized maximum shear force (P_m/P_0) decreases.

4.1.13 Relationship of k and P_m/P_0

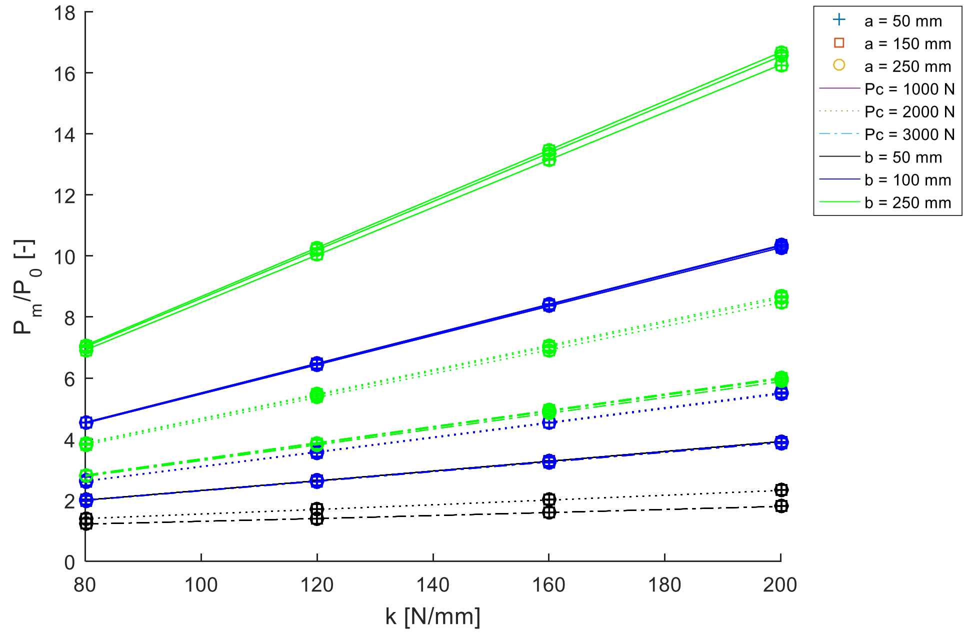

Figure 4.13 Relationship of k and P_m/P_0

Figure 4.13 shows the influence of the pivot plate dimension b, the pre-compressed load (P_C) and the spring stiffness (k) on the normalized maximum shear force (P_m/P_0). With the increase of the pivot plate dimension b and spring stiffness (k), the normalized maximum shear force (P_m/P_0) increases. With the increase of the pre-compressed load (P_C), the normalized maximum shear force (P_m/P_0) decreases.

4.1.14 Relationship of a and P_m/P_0

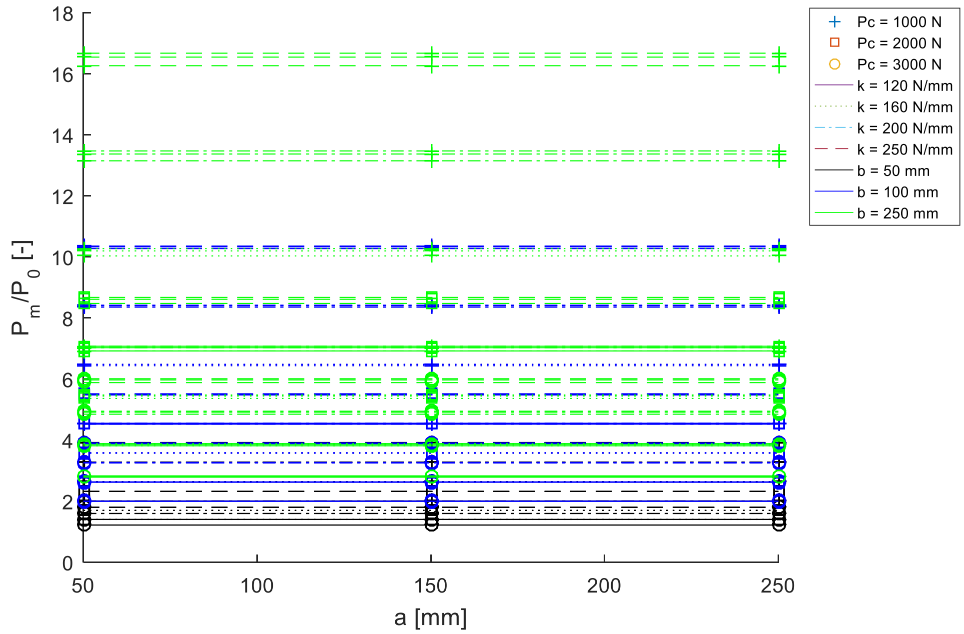

Figure 4.14 Relationship of a and P_m/P_0

Figure 4.14 shows the influence of the pivot plate dimension a and b, the pre-compressed load (P_C), and spring stiffness (k) on the normalized maximum shear force (P_m/P_0). When the a increases from 50mm to 250mm, the normalized maximum shear force (P_m/P_0) doesn't change much. Thus, the normalized maximum shear force (P_m/P_0) is independent of the pivot plate dimension a. With the increase of the pivot plate dimension b and spring stiffness (k), the normalized maximum shear force (P_m/P_0) increases. With the increase of the pre-compressed load (P_C), the normalized maximum shear force (P_m/P_0) decreases.

4.1.15 Relationship of b and P_m/P_0

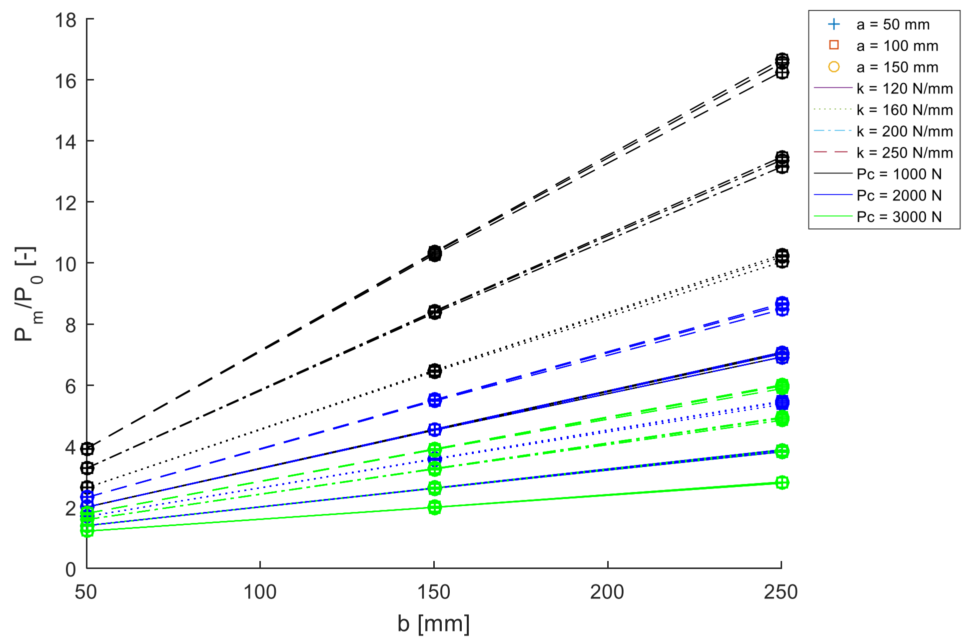

Figure 4.15 Relationship between b and P_m/P_0

Figure 4.15 shows the influence of the pivot plate dimension b, the pre-compressed load (P_C) and the spring stiffness (k) on the normalized maximum shear force (P_m/P_0). With the increase of the pivot plate dimension b and spring stiffness (k), the normalized maximum shear force (P_m/P_0) increases. With the increase of the pre-compressed load (P_C), the normalized maximum shear force (P_m/P_0) decreases.

4.2 Design approach

The SCNFD can be customized to satisfy different requirements for the structure seismic protection. Figure 4.16 shows the approach of optimal design. First, maximum drift ratio (δ_m) and the post stiffness (kp) are given by engineers to determine the shape of the hysteresis behavior. Secondly, the spring stiffness (k), dimensions in pivot plate and pre-compress load (P_C) can be tuned according to the given parameters. Then, the friction force (F_f) can be chosen to realize the energy dissipation capacity. After the expected flag-shaped behavior is obtained, the size of springs such as outer diameter, free length can be obtained from spring stores. With the dimension of spring, the dimension of spring cases can be determined. Then the dimension b should be checked to make sure during the motion, there is no collision happens between two spring cases. With the value of maximum drift ratio (δ_m) and the length of the SCNFD (a+L), the maximum displacement ($\triangle_m$) can be obtained. Then the length of the slotted hole in Plate A should be at least $2\triangle_m$. Figure 4.17 shows the dimension of the SCNFD. The length should be larger than (a+L) and the height should be larger than ($2b+4\triangle_m$). Figure 4.17 shows the dimension reference of the SCNFD.

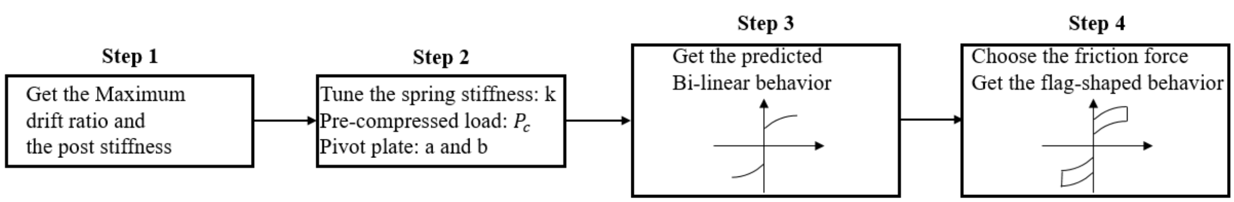

Figure 4.16 Flow chart of optimal design approach

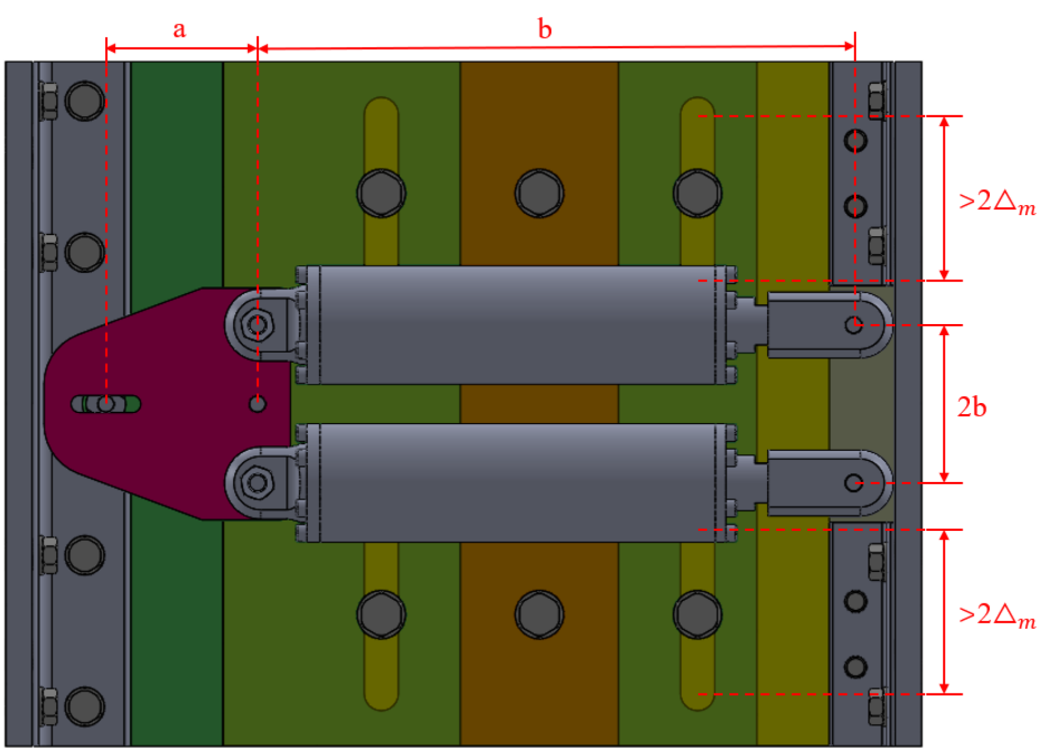

Figure 4.17 Dimension reference

4.3 Summary

This chapter presents the parameter study to investigate the influences of the flag-shaped behavior cause by pivot plate dimension a and b, the pre-compressed load (P_C), the spring stiffness (k) on the post stiffness (kp) and the initial length of the spring case (L). In the end, an optimal design approach is proposed for further customized damper design.

Chapter 5: Summary and conclusions

5.1 Conclusion

In recent earthquakes, the structures followed the conventional design philosophy didn't collopse but were subjected to permanent deformation due to plastic yielding. The residual drift may lead to a complete loss of the structure from an economic perspective and bring potential risk to the users. Thus, time-consuming replacement and repairment procedure need to be done. With the increasing requirement for the low residual drift in structural after earthquake, developing self-centering energy dissipation device is becoming a crucial need for high performance structure. However, conventional self-centering energy dissipation dampers usually have some drawbacks, such as undesirable interactions in post-tensioned damper, leakage in viscous damper and elastic "post yield" stiffness in spring damper. Those problems could lead damage to damper itself and structures. To avoid those problems, an idea of no-damage and nonliear mechanism has been raised. In this thesis, a novel self-centering nonlinear friction damper (SCNFD) is proposed. SCNFD utilizes pivot hinge, specially designed grove plates and pre-compressed springs to achieve self-centering nonlinear force-deformation response with no damage and avoid the linearly increases of the force as the deformation increases. The vertical deformation of the damper is transferred by pivot plates to axial deformation of springs. There are two pre-compressed springs connect to the pivot plate. When the pivot plate rotates, springs will bring the pivot plate back to the initial state. Besides, the spring stiffness and pre-compressed load can be easily changed according to different requirements. Detailed theoretical equations have been derived to describe the mechanism of the SCNFD by using the equilibrium equations of the pivot plate. The flag-shaped behavior of the SCNFD can be regarded as the superposition of the self-centering backbone and friction force. The theoretical equations of the self-centering mechanism were first verified by finite element model in ABAQUS. The ABAQUS model consists of a pivot plate and two pre-compressed springs. The self-centering backbone which perfectly matched with the theoretical equations was obtained by applying cyclic displacement to the bolt on Plate A. Then, the nonlinear behavior of the SCNFD was verified again by cyclic experimental tests in the Structural Engineering Laboratory at the University of British Columbia, Vancouver. Nine different configurations of SCNFD with different springs, pre-compressed load and friction force have been tested. The results show the theoretical equations have a good prediction for the behavior of the SCNFD. Besides, the SCNFD has a stable and predictable self-centering and energy dissipated behavior. It should be noted that, the post stiffness of the SCNFD decreases with the increasing of the displacement. Thus, the maximum deformation should be selected when the post stiffness equals to zero. Otherwise, negative stiffness will happen and may cause damage to structures. A detailed parameter study was carried out to examine influence of the sping stiffness (k), pre-compressed load (P_C), the initial length of the spring case (L), and pivot plate dimension a, b of the SCNFD. Based on the varified theoretical equations. The results of parameter study show the nonlinear behavior of the SCNFD is related to spring stiffness (k), pre-compressed load (P_C), the initial length of the spring case (L), and pivot plate dimension a, b. The post stiffness (kp) increases with the decreasing of a and increasing of b and spring stiffness (k). The maximum drift ratio ($\triangle_m$) increases with the increasing of a, b and spring stiffness (k). The normalized maximum shear force (P_m/P_0) increases with the increasing of pivot plate dimension b and spring stiffness (k) and decreasing of the pre-compressed load (P_C). The initial length of the spring case (L) and pivot dimension a don't have much effect on the normalized maximum shear force (P_m/P_0). The SCNFD is customized to satisfy different seismic protection requirements. The study has validated the

SCNFD as a stable self-centing and energy dissipation damper, which can be used in the seismic protection of stuctures.

Furthermore, an optimal design approach is proposed.

5.2 Future work

The results of this study show that SCNFD is a reliable and predictable nonlinear damper. This research mainly focuses on the proposed concept, mechanism design, theoretical equations and experimental test. The behavior and application should be investigated in further study. There are some recommendations for future studies.

- Because of the material restriction, springs have a limited travel length. In further research, springs with larger travel length needed to be found to achieve a better behavior.
- More experimental tests are needed to test more combinations of springs and pre-compress load.
- This study only focuses on component level. The seismic reaction of the structure with the SCNFD has not been studied. The structural seismic response needs to be carried out on system level to evaluate the effect of the SCNFD protection through numerical simulation.

Bibliography

Soong, T. T., & Dargush, G. F. (1998). Passive energy dissipation systems in structural engineering. *Structural Safety*, 20(2), 197-198.

Sahoo, D. R., & Rai, D. C. (2009). A Novel Technique of Seismic Strengthening of Nonductile RC Frame using Steel Caging and Aluminum Shear Yielding Damper. *Eathquake Spectre*, 25, 415-437.

Shahram, L. M., Hossein, T. R., & Mahmoud, H. (2019). Investigating the analytical and experimental performance of a pure torsional yielding damper. *Journal of Constructional Steel Research*, 161, 385-399.

Garivani, S., Aghakouchak, A. A., & Shahbeyk, S. (2019). Seismic Behavior of Steel Frames Equipped with Comb-Teeth Metallic Yielding Dampers. *International Journal of Steel Structures*, 19(4), 1070–1083.

Symans, M. D., & Constantinou, M. C. (1995). Development and experimental study of semi-active fluid damping devices for seismic protection of structures. *National Center for Earthquake Engineering Research*.

Hazaveh, N. K., Rodgers, G. W., Chase, J. G., & Pampanin, S. (2017). Experimental Test and Validation of a Direction- and Displacement-Dependent Viscous Damper. *Journal of Engineering Mechanics*, 143(11).

Naeem, A., & Kim, J. (2018). Seismic performance evaluation of a spring viscous damper cable system. *Engineering Structures*, 176, 455-467.

Ricles, J. M., Sause, M., Garlock, M. M., & Zhao, C. (2001). Posttensioned seismic-resistant connections for steel frames. J*ournal of Structural Engineering*, 127(2), 113-121.

Garlock, M. M., Ricles, J. M., & Sause, M. (2005). Experimental studies of full-scale posttensioned steel connections. *Journal of Structural Engineering*, 131(3), 438-448.

Chi, H., & Liu, J. (2012). Seismic behavior of post-tensioned column base for steel self-centering moment resisting frame. *Journal of Constructional Steel Research*, 78, 117-130.

Khoo, H. H., Clifton, C., Butterworth, J., MacRae, G., Gledhill, S., & Sidwell, G. (2012). Development of the self-centering Sliding Hinge Joint with friction ring springs. *Journal of Constructional Steel Research*, 78, 201-211.

Tremblay, M. (2001). Passive energy dissipation device for typical steel frame building in Iran. *Engineering Structures*, 23(6), 643-655.

Lin, Y. Y., Tsai, M. H., Hwang, J. S., & Chang, K. C. (2003). Direct displacement-based design for building with passive energy dissipation systems. *Engineering Structures*, 25(1), 25-37.

Xu, Z., Agrawal, A. K., He, W. L., & Tan, P. (2007). Performance of passive energy dissipation systems during near-field ground motion type pulses. *Engineering Structures*, 29(2), 224-236.

Tremblay, R., Merzouq, S., Izvernari, C., & Alexieva, K. (2005). Application of the equivalent static force procedure for the seismic design of multistorey buildings with vertical mass irregularity. *Canadian Journal of Civil Engineering*, 32(3), 561-568.

Kelly, J. M., Skinner, R. I., & Heine, A. J. (1972). Mechanisms of energy absorption in special devices for use in earthquake resistant structures. *New Zealand Society for Earthquake Engineering*, 5(3), 63-88.

Su, Y. F. (1990). Seismic response of building structures with mechanical damping devices. *University of Michigan*.

TahamouliRoudsari, M., Cheraghi, K., & Habibi, M. R. (2019). Investigation of retrofitting RC moment resisting frames with ADAS yielding dampers. *Asian Journal of Civil Engineering*, 20(1), 125-133.

Chan, R. W. K., & Albermani, K. (2008). Experimental study of steel slit damper for passive energy dissipation. *Engineering Structures*, 30(4), 1058-1066.

Qu, B., Dai, C. X., Qiu, J., Hou, H. T., & Qiu, C. X. (2019). Testing of seismic dampers with replaceable U-shaped steel plates. *Engineering Structures*, 179, 625-639.

Li, T. Y. (2018). Experimental testing and numerical modelling of honeycomb structural fuse. *University of British Columbia*

Graesser, E. J., & Cozzarelli, F. A. (1991) Shape-Memory Alloys as New Materials for Aseismic Isolation. *Journal of Engineering Mechanics*, 117(11), 2590-2608.

Hazaveh, N. K., Rodgers, G. W., Chase, J. G., & Pampanin, S. (2017). Experimental Test and Validation of a Direction and Displacement-Dependent Viscous Damper. *Journal of Engineering Mechanics*, 143(11), 4017132.

Naeem, A., & Kim, J. (2018). Seismic performance evaluation of a spring viscous damper cable system. *Engineering Structures,* 176, 455-467.

Ibrahim, R. A. (1994). Friction-induced vibration, chatter, squeal, and chaos Part II: Dynamics and modeling. *Applied Mechanics Review,* 47 (7), 227–253.

Symans, M. D., & Constantinou, M. C. (1998). Passive fluid viscous damping systems for seismic energy dissipation. *Journal of Earthquake Technology,* 35(4), 185-206.

Pall, A. S., & Marsh, C. (1982). Seismic Response of Friction Damped Braced Frames. *Journal of the Structure Devision*, 108(6), 1313-1323.

Hartog, J. P. (1931). Forced vibrations with combined Coulomb and viscousfriction. *Transactions of the American Society of Mechanical Engineers*, 53, 107–115.

Levitan, E. S. (1960). Forced oscillation of a spring-mass system having combined Coulomb and viscous damping. *Transactions of the American Society of Mechanical Engineers,* 32, 1265–1269.

Hundal, M. S. (1979). Response of a base excited system with Coulomb and viscous friction. *Journal of Sound and Vibration,* 64, 371–378.

Clifton, G. C. (2005). Semi-rigid joints for moment-resisting steel framed seismic-resisting systems. *The University of Auckland*

Hatami, M. (2019). Numerical and experimental study on friction connections performance-asymmetric and symmetric (AFC/SFC).

Mualla, I. H., & Belev, B. (2002). Performance of steel frames with a new friction damper device under earthquake excitation. *Engineering Structures*, 24(3), 365-371.

Golondrino, J. C., Macrae, G. A., & Chase, J. G. (2012). Clamping Force Effects on the Behaviour of Asymmetrical Friction Connections (AFC). *The 15th World Conference on Earthquake Engineering (15WCEE)*, Lisbon, Portugal.

Jeong, K., Choi, E., Back, S. Y., & Kang, J. W. (2016). Smart damper using sliding friction of aramid brake lining and self-centering of rubber springs. *International Journal of Steel Structures*, 16(4), 1239-1250.

Xu, L. H., Fan, X. W., & Li, Z. X. (2018). Development and experimental study of a self-centering variable damping energy dissipation brace. *Engineering Structures*, 160, 270-280.

Kim, H. J. & Christopoulos, C. (2008). Friction Damped Posttensioned Self-Centering Steel Moment-Resisting Frames. *Journal of Structural Engineering*, 134(11), 1768-1779.

Zhang, A. L., Zhang, Y. X., LI, R., & Wang, Z. Y. (2016). Cyclic behavior of a prefabricated self-centering beam–column connection with a bolted web friction device. *Engineering Structures*, 111, 185-198.

Appendices

Appendix A: Derivation of Fy

The derivation of Fy is conducted in Maple 2020.

```
restart;
alpha := arctan(delta/a) :
Dx1 := b·sin(alpha) :
Dx2 := Dx1 :
Dy1 := b − b·cos(alpha) :
Dy2 := Dy1 :
F1 := 2·k·(sqrt((L + Dx1)^2 + (Dy1)^2) − L) + 2·P :
F1_simplify := simplify(F1, symbolic) :
F1_ddelta := d/dδ(F1_simplify) :
F1_ddelta_simplify := simplify(F1_ddelta, sqrt, symbolic) :
F2 := 2·k·(L−sqrt((L − Dx2)^2 + (Dy2)^2)) + 2·P :
F2_simplify := simplify(F2, symbolic) :
F2_ddelta := d/dδ(F2_simplify) :
F2_ddelta_simplify := simplify(F2_ddelta, sqrt, symbolic) :
cos_beta1 := cos(arctan(Dy1/(L + Dx1))) :
cos_beta1_simplify := simplify(cos_beta1, symbolic) :
cos_beta1_ddelta := d/dδ(cos_beta1_simplify) :
cos_beta1_ddelta_simplify := simplify(cos_beta1_ddelta, symbolic) :
sin_beta1 := sin(arctan(Dy1/(L + Dx1))) :
sin_beta1_simplify := simplify(sin_beta1, symbolic) :
sin_beta1_ddelta := d/dδ(sin_beta1_simplify) :
sin_beta1_ddelta_simplify := simplify(sin_beta1_ddelta, symbolic) :
cos_beta2 := cos(arctan(Dy2/(L − Dx2))) :
cos_beta2_simplify := simplify(cos_beta2, symbolic) :
cos_beta2_ddelta := d/dδ(cos_beta2_simplify) :
cos_beta2_ddelta_simplify := simplify(cos_beta2_ddelta, symbolic) :
sin_beta2 := sin(arctan(Dy2/(L − Dx2))) :
sin_beta2_simplify := simplify(sin_beta2, symbolic) :
sin_beta2_ddelta := d/dδ(sin_beta2_simplify) :
sin_beta2_ddelta_simplify := simplify(sin_beta2_ddelta, symbolic) :
F1x := (F1_simplify)·(cos_beta1) :
F1y := (F1_simplify)·(sin_beta1) :
F1x_simplify := simplify(F1x, symbolic) :
F1y_simplify := simplify(F1y, symbolic) :
F2x := F2·(cos_beta2) :

F2y := F2·(sin_beta2) :
F2x_simplify := simplify(F2x, symbolic) :
F2y_simplify := simplify(F2y, symbolic) :
```

$F1x\_ddelta := F1\_ddelta\_simplify \cdot (cos\_beta1) + F1 \cdot (cos\_beta1\_ddelta\_simplify):$
$F1x\_ddelta\_simplify := simplify(F1x\_ddelta, symbolic):$
$F1y\_ddelta := F1\_ddelta\_simplify \cdot (sin\_beta1) + F1 \cdot (sin\_beta1\_ddelta\_simplify):$
$F1y\_ddelta\_simplify := simplify(F1y\_ddelta, symbolic):$
$F2x\_ddelta := F2\_ddelta\_simplify \cdot (cos\_beta2) + F2 \cdot (cos\_beta2\_ddelta\_simplify):$
$F2x\_ddelta\_simplify := simplify(F2x\_ddelta, symbolic):$
$F2y\_ddelta := F2\_ddelta\_simplify \cdot (sin\_beta2) + F2 \cdot (sin\_beta2\_ddelta\_simplify):$
$F2y\_ddelta\_simplify := simplify(F2y\_ddelta, symbolic):$
$A := r \cdot F1x\_ddelta\_simplify \cdot (\cos(\mathrm{alpha}))^3:$
$AA := simplify(A, symbolic):$
$cos\_alpha3\_ddelta := \frac{d}{d\,\mathrm{delta}}\left((\cos(\mathrm{alpha}))^3\right):$
$B := r \cdot F1x\_simplify \cdot cos\_alpha3\_ddelta:$
$BB := simplify(B, symbolic):$
$C := r \cdot F2x\_ddelta\_simplify \cdot (\cos(\mathrm{alpha}))^3:$
$CC := simplify(C, symbolic):$
$DD := r \cdot F2x \cdot cos\_alpha3\_ddelta:$

$DD\_simplify := simplify(DD, symbolic):$
$sin\_2alpha\_ddelta := \frac{d}{d\,\mathrm{delta}}((\sin(2 \cdot \mathrm{alpha}))):$
$sin\_2alpha\_ddelta\_simplify := simplify(sin\_2alpha\_ddelta, trig):$
$cos\_alpha\_ddelta := \frac{d}{d\,\mathrm{delta}}(\cos(\mathrm{alpha})):$
$cos\_alpha\_ddelta\_simplify := simplify(cos\_alpha\_ddelta, symbolic):$
$E := \frac{r}{2} \cdot sin\_2alpha\_ddelta\_simplify \cdot \cos(\mathrm{alpha}) \cdot F1y\_simplify:$
$EE := simplify(E, symbolic):$
$F := \frac{r \cdot \sin(2 \cdot \mathrm{alpha})}{2} \cdot cos\_alpha\_ddelta\_simplify \cdot F1y\_simplify:$
$FF := simplify(F, symbolic):$
$G := \frac{r \cdot \sin(2 \cdot \mathrm{alpha})}{2} \cdot \cos(\mathrm{alpha}) \cdot F1y\_ddelta\_simplify:$
$GG := simplify(G, symbolic):$
$H := -\frac{r}{2} \cdot sin\_2alpha\_ddelta\_simplify \cdot \cos(\mathrm{alpha}) \cdot F2y\_simplify:$
$HH := simplify(H, symbolic):$
$II := -\frac{r \cdot \sin(2 \cdot \mathrm{alpha})}{2} \cdot cos\_alpha\_ddelta\_simplify \cdot F2y\_simplify:$
$II\_simplify := simplify(II, symbolic):$
$J := -\frac{r \cdot \sin(2 \cdot \mathrm{alpha})}{2} \cdot \cos(\mathrm{alpha}) \cdot F2y\_ddelta\_simplify:$

$JJ := simplify(J,\ symbolic):$
$K\ :=\ AA + BB + CC + DD\_simplify + EE + FF + GG + HH + II\_simplify + JJ$

$$K := \frac{2\,r\,a^4\left(a\left(2\,L\,b\,\delta-2\,a\,b^2+\left(L^2+2\,b^2\right)\sqrt{a^2+\delta^2}\right)k\sqrt{\left(2\,L\,b\,\delta-2\,a\,b^2\right)\sqrt{a^2+\delta^2}+\left(a^2+\delta^2\right)\left(L^2+2\,b^2\right)}+\left(\left(\left(2\,a^2+\delta^2\right)b-L\,a\,\delta\right)\sqrt{a^2+\delta^2}+\left(a^2+\delta^2\right)\left(L\,\delta-2\,a\,b\right)\right)\left(k\,L-P\right)b\right)b}{\left(a^2+\delta^2\right)^{5/2}\left(\left(2\,L\,b\,\delta-2\,a\,b^2\right)\sqrt{a^2+\delta^2}+\left(a^2+\delta^2\right)\left(L^2+2\,b^2\right)\right)^{3/2}}$$

$$+\frac{6\,\delta\,r\left(\sqrt{a^2+\delta^2}\,L+b\,\delta\right)a^3\left(-k\sqrt{\left(2\,L\,b\,\delta-2\,a\,b^2\right)\sqrt{a^2+\delta^2}+\left(a^2+\delta^2\right)\left(L^2+2\,b^2\right)}+\sqrt{a^2+\delta^2}\,\left(k\,L-P\right)\right)}{\sqrt{\left(2\,L\,b\,\delta-2\,a\,b^2\right)\sqrt{a^2+\delta^2}+\left(a^2+\delta^2\right)\left(L^2+2\,b^2\right)}\,\left(a^2+\delta^2\right)^3}$$

$$+\frac{2\,r\,a^4\,b\left(\left(-2\,L\,b\,\delta-2\,a\,b^2+\left(L^2+2\,b^2\right)\sqrt{a^2+\delta^2}\right)a\,k\sqrt{\left(-2\,L\,b\,\delta-2\,a\,b^2\right)\sqrt{a^2+\delta^2}+\left(a^2+\delta^2\right)\left(L^2+2\,b^2\right)}-\left(\left(\left(-2\,a^2-\delta^2\right)b-L\,a\,\delta\right)\sqrt{a^2+\delta^2}+\left(a^2+\delta^2\right)\left(L\,\delta+2\,a\,b\right)\right)\left(k\,L+P\right)b\right)}{\left(a^2+\delta^2\right)^{5/2}\left(\left(-2\,L\,b\,\delta-2\,a\,b^2\right)\sqrt{a^2+\delta^2}+\left(a^2+\delta^2\right)\left(L^2+2\,b^2\right)\right)^{3/2}}$$

$$-\frac{6\left(\sqrt{a^2+\delta^2}\,L-b\,\delta\right)\delta\,r\,a^3\left(-k\sqrt{\left(-2\,L\,b\,\delta-2\,a\,b^2\right)\sqrt{a^2+\delta^2}+\left(a^2+\delta^2\right)\left(L^2+2\,b^2\right)}+\left(k\,L+P\right)\sqrt{a^2+\delta^2}\right)}{\sqrt{\left(-2\,L\,b\,\delta-2\,a\,b^2\right)\sqrt{a^2+\delta^2}+\left(a^2+\delta^2\right)\left(L^2+2\,b^2\right)}\,\left(a^2+\delta^2\right)^3}$$

$$+\frac{2\,r\,a^2\left(-\sqrt{a^2+\delta^2}+a\right)\left(-k\sqrt{\left(2\,L\,b\,\delta-2\,a\,b^2\right)\sqrt{a^2+\delta^2}+\left(a^2+\delta^2\right)\left(L^2+2\,b^2\right)}+\sqrt{a^2+\delta^2}\,\left(k\,L-P\right)\right)b\cos\left(2\arctan\left(\frac{\delta}{a}\right)\right)}{\sqrt{\left(2\,L\,b\,\delta-2\,a\,b^2\right)\sqrt{a^2+\delta^2}+\left(a^2+\delta^2\right)\left(L^2+2\,b^2\right)}\,\left(a^2+\delta^2\right)^2}$$

$$+\frac{\delta\,r\,a\left(-\sqrt{a^2+\delta^2}+a\right)b\left(\left(-k\,L+P\right)\sqrt{a^2+\delta^2}+k\sqrt{\left(2\,L\,b\,\delta-2\,a\,b^2\right)\sqrt{a^2+\delta^2}+\left(a^2+\delta^2\right)\left(L^2+2\,b^2\right)}\right)\sin\left(2\arctan\left(\frac{\delta}{a}\right)\right)}{\sqrt{\left(2\,L\,b\,\delta-2\,a\,b^2\right)\sqrt{a^2+\delta^2}+\left(a^2+\delta^2\right)\left(L^2+2\,b^2\right)}\,\left(a^2+\delta^2\right)^2}$$

$$-\frac{1}{\left(\left(2\,L\,b\,\delta-2\,a\,b^2\right)\sqrt{a^2+\delta^2}+\left(a^2+\delta^2\right)\left(L^2+2\,b^2\right)\right)^{3/2}\left(a^2+\delta^2\right)^{3/2}}\Bigg(r\Bigg(-\delta\left(2\,L\,b\,\delta-2\,a\,b^2+\left(L^2+2\,b^2\right)\sqrt{a^2+\delta^2}\right)k\sqrt{\left(2\,L\,b\,\delta-2\,a\,b^2\right)\sqrt{a^2+\delta^2}+\left(a^2+\delta^2\right)\left(L^2+2\,b^2\right)}+(k\,L$$
$$-P)\left(\left(L\,a^2+2\,L\,\delta^2-a\,\delta\,b\right)b\sqrt{a^2+\delta^2}+\left(\left(L^2+b^2\right)\delta-L\,a\,b\right)\left(a^2+\delta^2\right)\right)\Bigg)a^2\,b\sin\left(2\arctan\left(\frac{\delta}{a}\right)\right)\Bigg)$$

$$+\frac{2\,r\,a^2\left(-k\sqrt{\left(-2\,L\,b\,\delta-2\,a\,b^2\right)\sqrt{a^2+\delta^2}+\left(a^2+\delta^2\right)\left(L^2+2\,b^2\right)}+\left(k\,L+P\right)\sqrt{a^2+\delta^2}\right)\left(-\sqrt{a^2+\delta^2}+a\right)b\cos\left(2\arctan\left(\frac{\delta}{a}\right)\right)}{\sqrt{\left(-2\,L\,b\,\delta-2\,a\,b^2\right)\sqrt{a^2+\delta^2}+\left(a^2+\delta^2\right)\left(L^2+2\,b^2\right)}\,\left(a^2+\delta^2\right)^2}$$

$$+\frac{\delta\,r\,a\left(-\sqrt{a^2+\delta^2}+a\right)b\sin\left(2\arctan\left(\frac{\delta}{a}\right)\right)\left(\left(-k\,L-P\right)\sqrt{a^2+\delta^2}+k\sqrt{\left(-2\,L\,b\,\delta-2\,a\,b^2\right)\sqrt{a^2+\delta^2}+\left(a^2+\delta^2\right)\left(L^2+2\,b^2\right)}\right)}{\sqrt{\left(-2\,L\,b\,\delta-2\,a\,b^2\right)\sqrt{a^2+\delta^2}+\left(a^2+\delta^2\right)\left(L^2+2\,b^2\right)}\,\left(a^2+\delta^2\right)^2}$$

$$-\frac{1}{\left(\left(-2\,L\,b\,\delta-2\,a\,b^2\right)\sqrt{a^2+\delta^2}+\left(a^2+\delta^2\right)\left(L^2+2\,b^2\right)\right)^{3/2}\left(a^2+\delta^2\right)^{3/2}}\Bigg(r\,a^2\Bigg(-\left(-2\,L\,b\,\delta-2\,a\,b^2+\left(L^2+2\,b^2\right)\sqrt{a^2+\delta^2}\right)\delta\,k\sqrt{\left(-2\,L\,b\,\delta-2\,a\,b^2\right)\sqrt{a^2+\delta^2}+\left(a^2+\delta^2\right)\left(L^2+2\,b^2\right)}+\Big($$
$$-b\left(L\,a^2+2\,L\,\delta^2+a\,\delta\,b\right)\sqrt{a^2+\delta^2}+\left(a^2+\delta^2\right)\left(\left(L^2+b^2\right)\delta+L\,a\,b\right)\Big)\left(k\,L+P\right)\Bigg)b\sin\left(2\arctan\left(\frac{\delta}{a}\right)\right)\Bigg)$$

Appendix B: Linear pots calibration

The calibration of linear pots was conducted by using gage blocks, the reading value of the linear pots is the retracted length.

Figure A.1 Linear pot calibration

Calibration results for linear pots

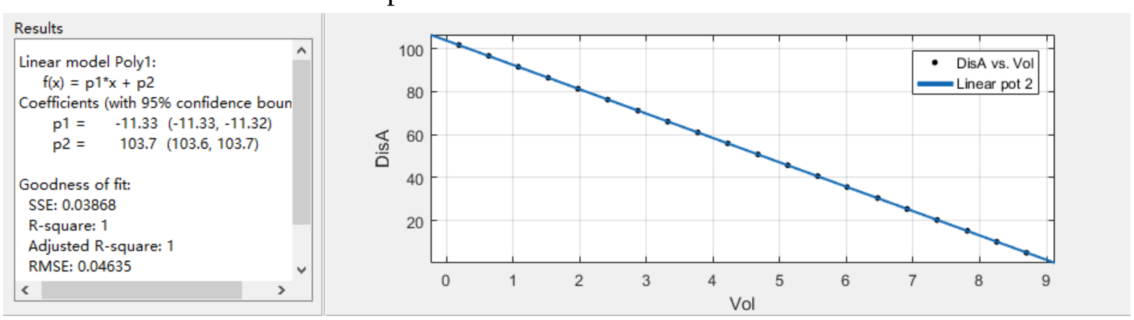

Figure A.2 Calibration result for linear pot 1

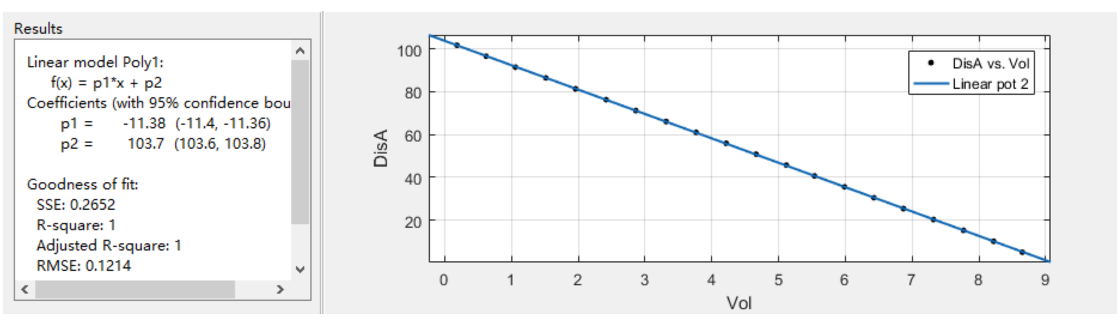

Figure A.3 Calibration result for linear pot 2

Appendix C: Linear pots reading values

Displacement records for two linear pots during each test:

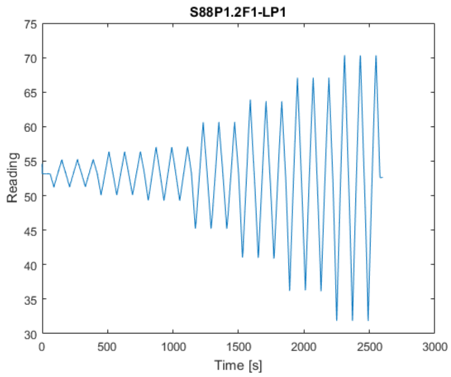

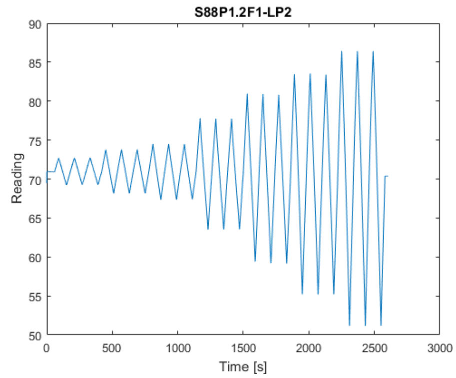

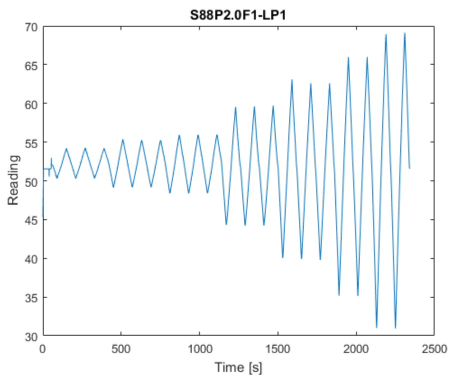

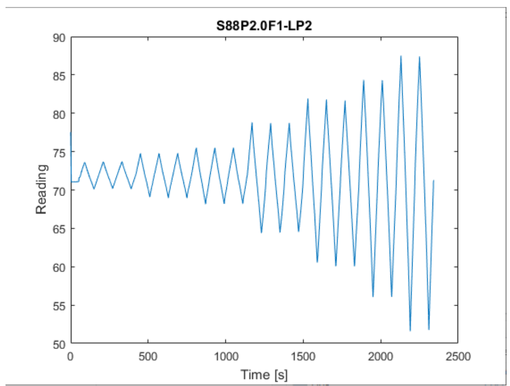

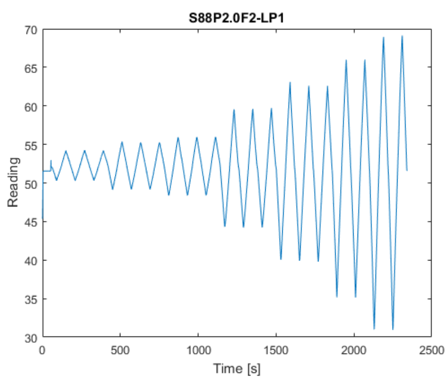

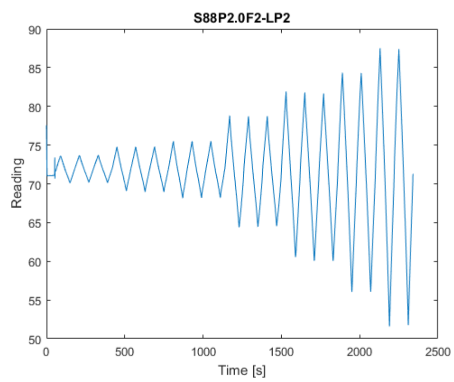

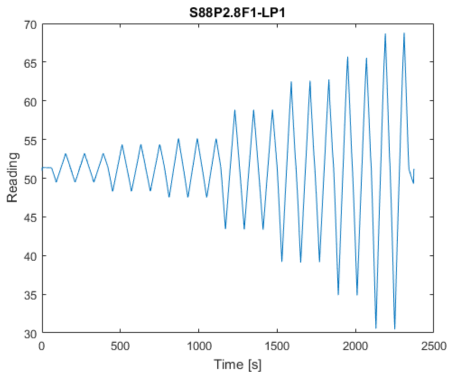
S88P2.8F1-LP1
Reading
Time [s]

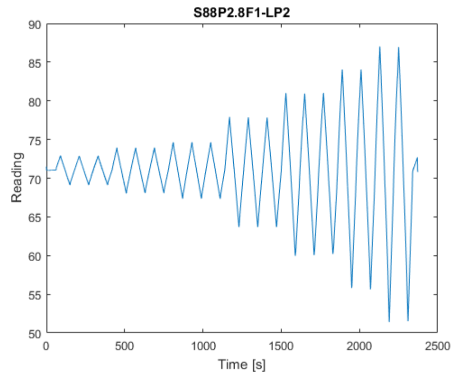
S88P2.8F1-LP2
Reading
Time [s]

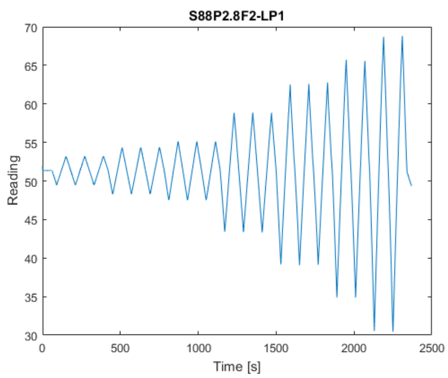
S88P2.8F2-LP1
Reading
Time [s]

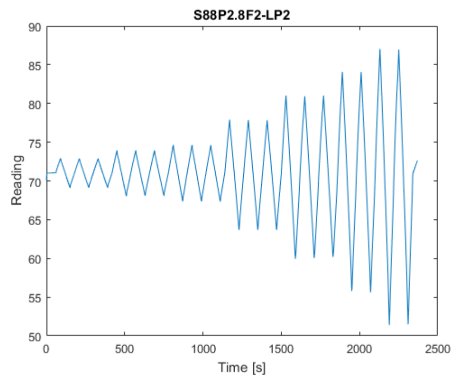
S88P2.8F2-LP2
Reading
Time [s]

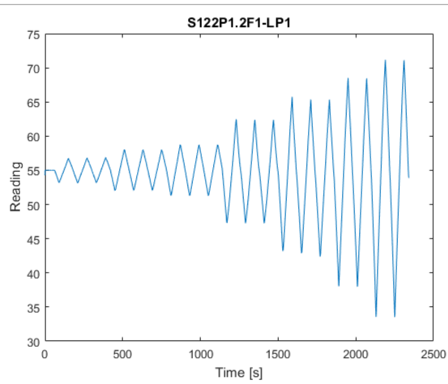
S122P1.2F1-LP1
Reading
Time [s]

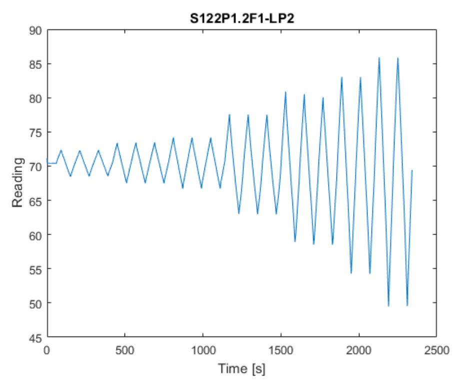
S122P1.2F1-LP2
Reading
Time [s]

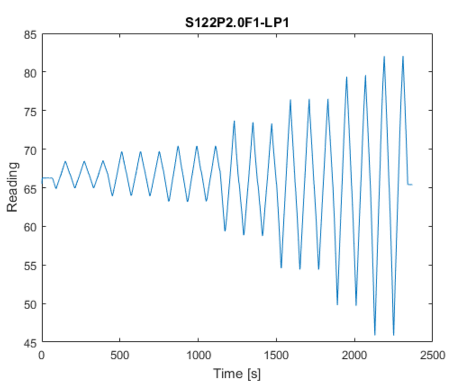
S122P2.0F1-LP1
Reading
Time [s]

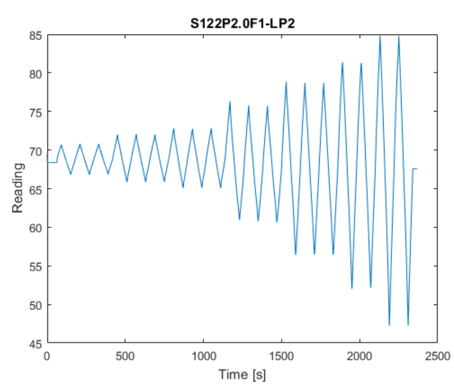
S122P2.0F1-LP2
Reading
Time [s]

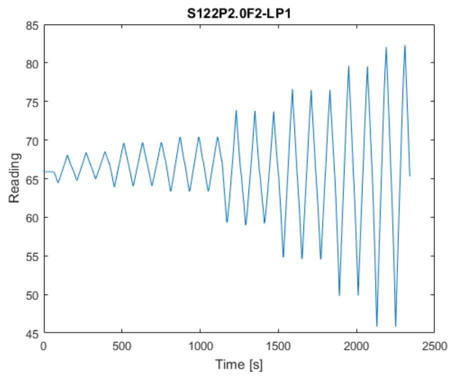
S122P2.0F2-LP1
Reading
Time [s]

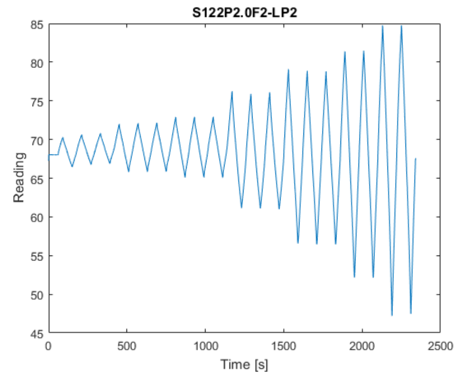
S122P2.0F2-LP2
Reading
Time [s]

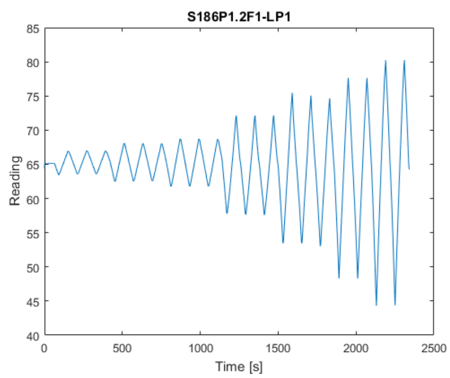
S186P1.2F1-LP1
Reading
Time [s]

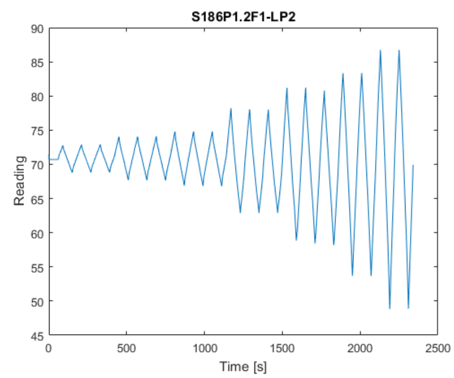
S186P1.2F1-LP2
Reading
Time [s]

Appendix D: Load cell reading values

Force records for load cell during each test:

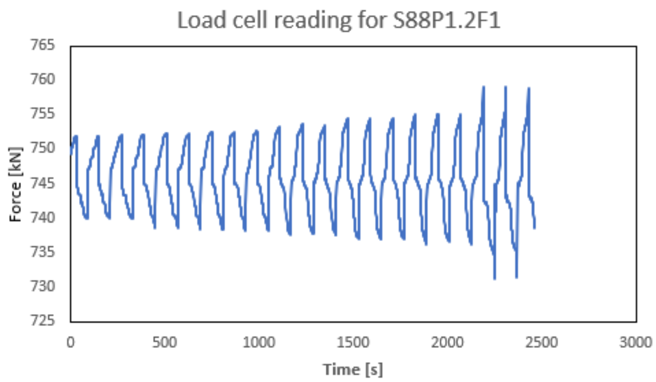

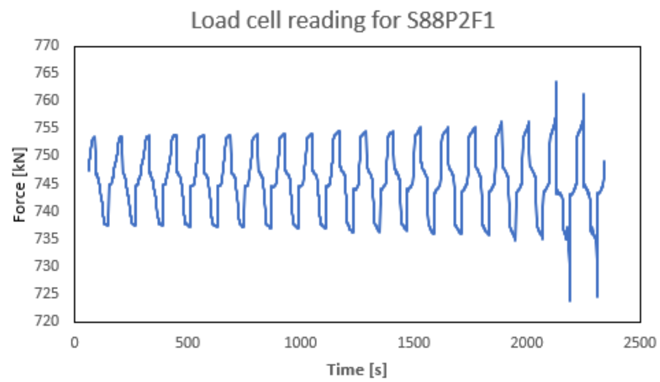

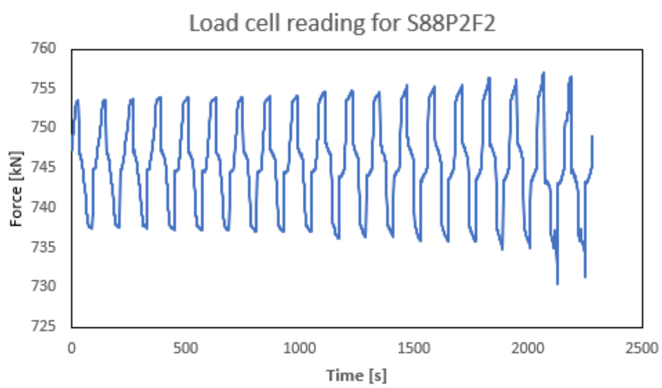

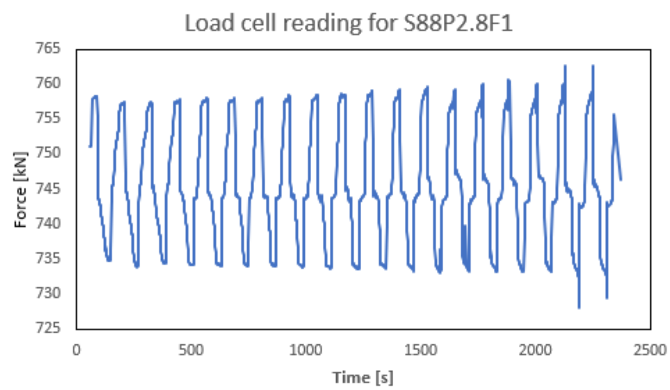

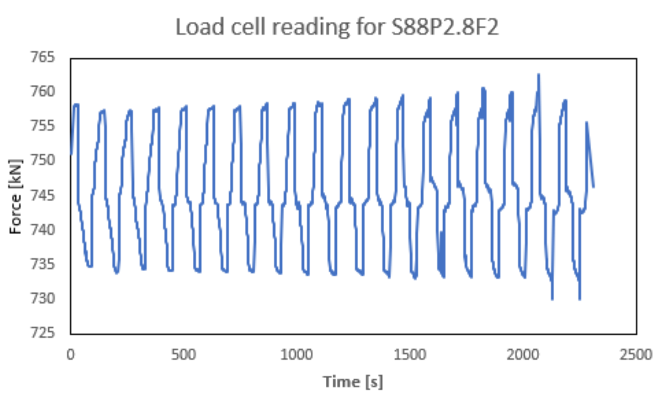

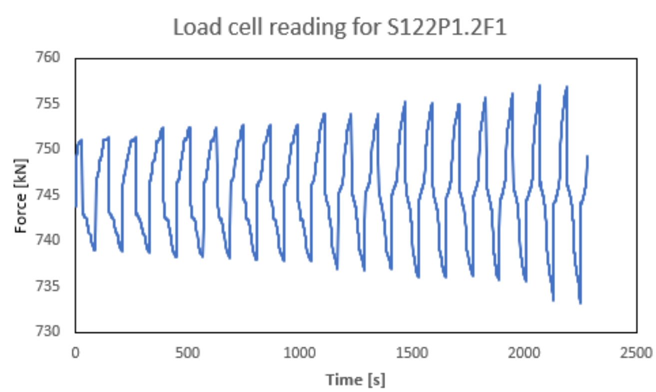

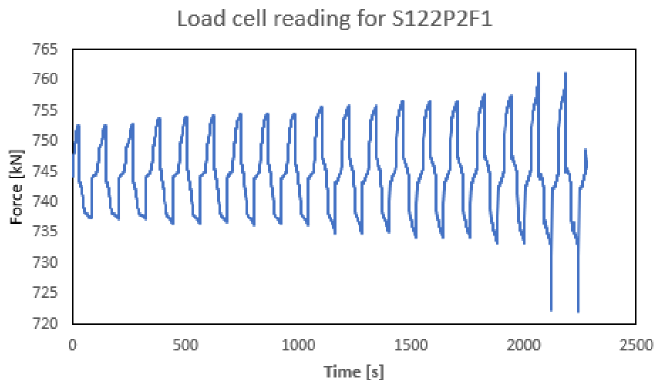
Load cell reading for S122P2F1
Force [kN]
Time [s]
765
760
755
750
745
740
735
730
725
720
0
500
1000
1500
2000
2500

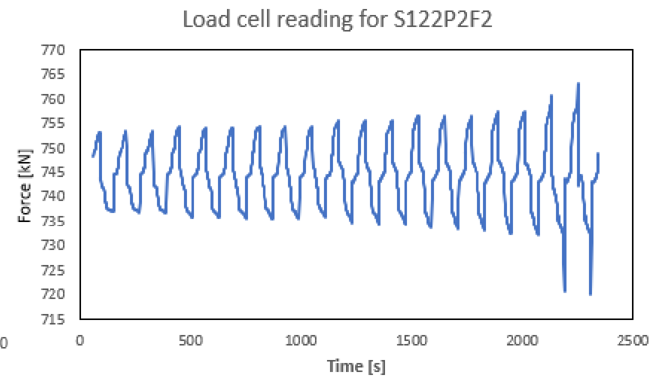
Load cell reading for S122P2F2
Force [kN]
Time [s]
770
765
760
755
750
745
740
735
730
725
720
715
0
500
1000
1500
2000
2500

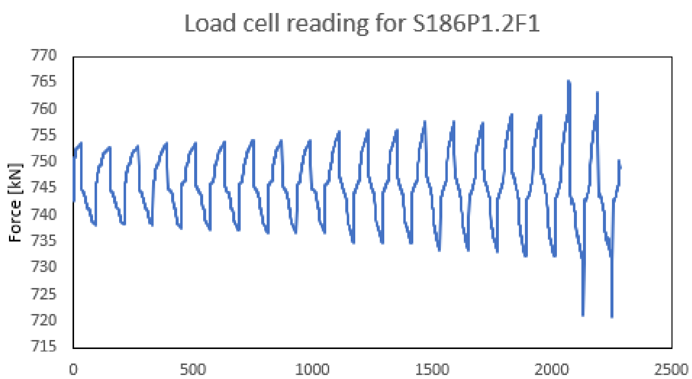
Load cell reading for S186P1.2F1
Force [kN]
770
765
760
755
750
745
740
735
730
725
720
715
0
500
1000
1500
2000
2500